bodies and embryos with the use of a novel microarray platform. Fertil Steril. 2014;102(5):1385–92. doi:10.1016/j.fertnstert.2014.07.1233 **Epub 2014 Sep 11.**

30. Mertzanidou A, Wilton L, Cheng J, Spits C, Vanneste E, Moreau Y, Vermeesch JR, Sermon K. Microarray analysis reveals abnormal chromosomal complements in over 70% of 14 normally developing human embryos. Hum Reprod. 2013;28(1):256–64. doi:10.1093/humrep/des362 **Epub 2012 Oct 9.**
31. Munné S, Velilla E, Colls P. Garcia Bermudez M, Vemuri MC, Steuerwald N, Garrisi J, Cohen J. Self-correction of chromosomally abnormal embryos in culture and implications for stem cell production. Fertil Steril. 2005;84(5):1328–34.
32. Barbash-Hazan S, Frumkin T, Malcov M, Yaron Y, Cohen T, Azem F, Amit A, Ben-Yosef D. Preimplantation aneuploid embryos undergo self-correction in correlation with their developmental potential. Fertil Steril. 2009;92(3):890–6. doi:10.1016/j.fertnstert.2008.07.1761 **Epub 2008 Sep 30.**
33. Novik V, Moulton EB, Sisson ME, Shrestha SL, Tran KD, Stern HJ, Mariani BD, Stanley WS. The accuracy of chromosomal microarray testing for identification of embryonic mosaicism in human blastocysts. Mol Cytogenet. 2014;7(1):18. doi:10.1186/1755-8166-7-18.
34. Van der Aa N, Cheng J, Mateiu L. Zamani Esteki M, Kumar P, Dimitriadou E, Vanneste E, Moreau Y, Vermeesch JR, Voet T. Genome-wide copy number profiling of single cells in S-phase reveals DNA-replication domains. Nucleic Acids Res. 2013;41(6):e66. doi:10.1093/nar/gks1352 **(epub 2013 Jan 7).**
35. Dimitriadou E, Van der Aa N, Cheng J, Voet T, Vermeesch JR. Single cell segmental aneuploidy detection is compromised by S phase. Mol Cytogenet. 2014;7:46. doi:10.1186/1755-8166-7-46 **(eCollection 2014).**
36. Northrop LE, Treff NR, Levy B, Scott RT Jr. SNP microarray-based 24 chromosome aneuploidy screening demonstrates that cleavage-stage FISH poorly predicts aneuploidy in embryos that develop to morphologically normal blastocysts. Mol Hum Reprod. 2010;16(8):590–600. doi:10.1093/molehr/gaq037 **(epub 2010 May 17).**
37. Warburton D, Dallaire L, Thangavelu M, Ross L, Levin B, Kline J. Trisomy recurrence: a reconsideration based on North American data. Am J Hum Genet. 2004;75(3):376–85 **Epub 2004 Jul 8.**
38. Rai R, Regan L. Recurrent miscarriage. Lancet. 2006;368(9535):601–11 **(review).**
39. Brezina PR, Brezina DS, Kearns WG. Preimplantation genetic testing. BMJ. 2012;18(345):e5908. doi:10.1136/bmj.e5908 **(review. No abstract available).**
40. Bolor H, Mori T, Nishiyama S, Ito Y, Hosoba E, Inagaki H, Kogo H, Ohye T, Tsutsumi M, Kato T, Tong M, Nishizawa H, Pryor-Koishi K, Kitaoka E, Sawada T, Nishiyama Y, Udagawa Y, Kurahashi H. Mutations of the SYCP3 gene in women with recurrent pregnancy loss. Am J Hum Genet. 2009;84(1):14–20. doi:10.1016/j.ajhg.2008.12.002 **Epub 2008 Dec 24.**
41. McCoy RC, Demko Z, Ryan A, Banjevic M, Hill M, Sigurjonsson S, Rabinowitz M, Fraser HB, Petrov DA. Common variants spanning PLK4 are associated with mitotic-origin aneuploidy in human embryos. Science. 2015;348(6231):235–8. doi:10.1126/science.aaa3337.
42. Stephenson M, Kutteh W. Evaluation and management of recurrent early pregnancy loss. Clin Obstet Gynecol. 2007;50(1):132–45 **(review).**
43. Voullaire L, Wilton L, McBain J, Callaghan T, Williamson R. Chromosome abnormalities identified by comparative genomic hybridization in embryos from women with repeated implantation failure. Mol Hum Reprod. 2002;8(11):1035–41.
44. Mastenbroek S, Twisk M, van Echten-Arends J, Sikkema-Raddatz B, Korevaar JC, Verhoeve HR, Vogel NE, Arts EG, de Vries JW, Bossuyt PM, Buys CH, Heineman MJ, Repping S, van der Veen F. In vitro fertilization with preimplantation genetic screening. N Engl J Med. 2007;357(1):9–17 **epub 2007 Jul 4.**
45. Moutou C, Goossens V, Coonen E, De Rycke M, Kokkali G, Renwick P, SenGupta SB, Vesela K, Traeger-Synodinos J. ESHRE PGD Consortium data collection XII: cycles from January to December 2009 with pregnancy follow-up to October 2010. Hum Reprod. 2014;29(5):880–903. doi:10.1093/humrep/deu012 **Epub 2014 Mar 11.**
46. Piazza R, Magistroni V, Pirola A, Redaelli S, Spinelli R, Redaelli S, Galbiati M, Valletta S, Giudici G, Cazzaniga G, Gambacorti-Passerini C. CEQer: a graphical tool for copy number and allelic imbalance detection from whole-exome sequencing data. PLoS ONE. 2013;8(10):e74825. doi:10.1371/journal.pone.0074825 **(eCollection 2013).**
47. Fan HC, Blumenfeld YJ, Chitkara U, Hudgins L, Quake SR. Noninvasive diagnosis of fetal aneuploidy by shotgun sequencing DNA from maternal blood. Proc Natl Acad Sci USA. 2008;105(42):16266–71. doi:10.1073/pnas.0808319105 **Epub 2008 Oct 6.**
48. Chiu RW, Chan KC, Gao Y, Lau VY, Zheng W, Leung TY, Foo CH, Xie B, Tsui NB, Lun FM, Zee BC, Lau TK, Cantor CR, Lo YM. Noninvasive prenatal diagnosis of fetal chromosomal aneuploidy by massively parallel genomic sequencing of DNA in maternal plasma. Proc Natl Acad Sci USA. 2008;105(51):20458–63. doi:10.1073/pnas.0810641105 **Epub 2008 Dec 10.**
49. Fiorentino F, Biricik A, Bono S, Spizzichino L, Cotroneo E, Cottone G, Kokocinski F, Michel CE. Development and validation of a next-generation sequencing-based protocol for 24-chromosome aneuploidy screening of embryos. Fertil Steril. 2014;101(5):1375–82. doi:10.1016/j.fertnstert.2014.01.051 **Epub 2014 Mar 6.**

Miyazaki et al. BMC Medical Genetics (2015) 16:98
DOI 10.1186/s12881-015-0245-3

BMC Medical Genetics

CASE REPORT Open Access

Intragenic duplication in the *PHKD1* gene in autosomal recessive polycystic kidney disease

Jun Miyazaki[1,2], Mayuko Ito[1,2], Haruki Nishizawa[2], Takema Kato[1], Yukito Minami[2], Hidehito Inagaki[1,3], Tamae Ohye[1,4], Masafumi Miyata[5], Hiroko Boda[5], Yuka Kiriyama[6], Makoto Kuroda[6], Takao Sekiya[2], Hiroki Kurahashi[1,3,4*] and Takuma Fujii[2]

Abstract

Background: In the present study, we report on a couple who underwent prenatal genetic diagnosis for autosomal recessive polycystic kidney disease (ARPKD).

Case presentation: This healthy couple had previously had a healthy boy but had experienced two consecutive neonatal deaths due to respiratory distress resulting from pulmonary hypoplasia caused by oligohydramnios. The woman consulted our facility after she realized she was pregnant again. We promptly performed a carrier test for the *PKHD1* gene by target exome sequencing of samples from the couple. A pathogenic mutation was identified only in the paternal allele (c.9008C>T, p.S3003F). The mutation was confirmed by Sanger sequencing of the DNA from formalin-fixed, paraffin-embedded, kidney tissue of the second neonate patient and was not found in the healthy sibling. We then performed haplotype analyses using microsatellite markers scattered throughout the *PKHD1* gene. DNA from the amniocentesis was determined to belong to a carrier, and the couple decided to continue with the pregnancy, obtaining a healthy newborn. Subsequent detailed examination of the exome data suggested higher read depth at exons 45 and 46. Multiplex ligation-dependent probe amplification allowed identification of duplication of these two exons. This case suggests the potential usefulness of target exome sequencing in the prenatal diagnosis of the *PKHD1* gene in ARPKD.

Conclusions: This is the first report of intragenic duplication in the *PKHD1* gene in ARPKD.

Keywords: ARPKD, Prenatal diagnosis, Target exome, *PKHD1*, Duplication

Background

Autosomal recessive polycystic kidney disease (ARPKD) is recognized as a severe hereditary form of polycystic kidney disease [MIM 263200]. Patients present with enlarged kidneys with dilatations of the collecting ducts and congenital hepatic fibrosis. Severely affected neonates have oligohydramnios and pulmonary hypoplasia that cause respiratory distress in the perinatal period. Approximately 30 % of affected children die within the first year of life [1]. Survivors of the perinatal respiratory insufficiency and cases with later onset generally progress to end-stage renal disease before adulthood. A minority of patients come to medical attention in adulthood with liver-related complications and mild kidney disease. ARPKD is a rare disorder that affects ~1 in 20,000 live births.

ARPKD is caused by mutations in the *PKHD1* gene, chromosomally located at 6p12.2 [2, 3]. The *PKHD1* gene is mainly expressed in the kidneys and liver, as well as the pancreas. The encoded fibrocystin/polyductin protein is a receptor-like transmembrane protein that localizes at primary cilium, particularly at the basal body of the cilium, and possibly functions as the sensory antenna in renal epithelial cells or biliary duct cells [4]. Biallelic truncating mutations or pathogenic missense mutations are identified in most ARPKD cases [5]. The *PKHD1* gene is considered the only gene with mutations causally associated with ARPKD.

The carrier test for ARPKD has conventionally been performed by Sanger sequencing of the *PKHD1* gene. However, this process is laborious and time-consuming because the *PKHD1* gene is a large gene spanning a 470-kb genomic region and consisting of 86 exons, including alternatively spliced exons [2, 3]. In prenatal diagnosis, each

* Correspondence: kura@fujita-hu.ac.jp
[1]Division of Molecular Genetics, Institute for Comprehensive Medical Science, Fujita Health University, 1-98 Dengakugakubo, Kutsukake-cho, Toyoake, Aichi 470-1192, Japan
[3]Genome and Transcriptome Analysis Center, Fujita Health University, Aichi, Japan
Full list of author information is available at the end of the article

mutation of the carrier parents needs to be determined within a short period. Denaturing high-performance liquid chromatography is one sequencing option to reduce time and cost, although it is difficult to find the conditions for optimal sensitivity [6, 7]. Recent advances in next-generation sequencing have allowed *PKHD1* mutations to be screened with exome sequencing [8]. In our present report, we describe carrier testing using target exome sequencing performed for prenatal diagnosis. In addition, we report a rare intragenic duplication in the *PKHD1* gene in ARPKD.

Methods

Human samples

In this study, we used genomic DNA samples from members of a Japanese family with ARPKD siblings (Fig. 1). After informed consent was provided, peripheral blood samples were obtained. Genomic DNA was purified by QuickGene-610 L (Fuji Film). In addition, we extracted DNA from formalin-fixed, paraffin-embedded (FFPE), kidney tissue from one of the ARPKD neonatal patients with the aid of QIAamp DNA FFPE Tissue (Qiagen). This study was approved by the Ethical Review Board for Human Genome Studies of Fujita Health University (accession number 13-14; approved on September 24, 2013).

Next-generation sequencing

For target exome sequencing, libraries were prepared using the TruSight Rapid Capture kit (Illumina) according to the manufacturer's specifications. After tagmentation with transposase, the libraries were amplified to add indices and common adapters for subsequent cluster generation and sequencing. The libraries were quantified by a 2100 Bioanalyzer (Agilent Technologies) using the High Sensitivity DNA Kit (Agilent Technologies, 5067–4626). Next, exon capture was performed using a TruSight Inherited Disease Panel (Illumina, TG141–1005). Prior to cluster generation, the libraries were further quantified by Qubit (Invitrogen, Q32866) using the Qubit dsDNA HS Assay Kit (Invitrogen, Q32851). Finally, the prepared library was loaded on an Illumina MiSeq clamshell-style cartridge for paired-end sequencing (Illumina). The data were analyzed with the aid of Variant Studio for filtering and annotation (Illumina). The reads were reanalyzed for copy number alterations using the Comparative Exome Quantification analyzer CEQer [9].

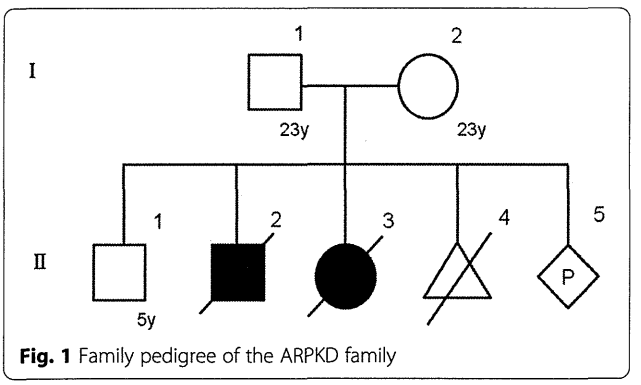

Fig. 1 Family pedigree of the ARPKD family

Microsatellite analyses

A total of seven microsatellite markers were selected based on previous reports (Table 1) [10, 11]. Forward primers were labeled with FAM. The PCR products were analyzed by capillary electrophoresis (ABI3730 Genetic Analyzer; Applied Biosystems).

Multiplex ligation-dependent probe amplification

Multiplex ligation-dependent probe amplification (MLPA) probe pairs for the *PHKD1* gene were used (SALSA MLPA probe mix P341/P342; MRC-Holland, Amsterdam, the Netherlands). In this approach, the MLPA probes consist of two oligonucleotides, each containing a PCR primer sequence and a variable length sequence complementary to the target. Genomic DNA was denatured (1 min at 98 °C) and subsequently hybridized to the MLPA probe pairs in accordance with the manufacturer's protocol. After ligation, probe pairs were amplified using universal primers. The multiplex PCR products were then separated on a capillary sequencer (ABI3730 Genetic Analyzer).

PCR amplification of the junction fragments

To isolate junction fragments, PCR was performed using ExTaq (TaKaRa, Shiga, Japan). The PCR conditions were 35 cycles of 10 s at 98 °C and 3.5 min at 60 °C. PCR primers were designed using sequence data from the human genome database. The following primers were used for amplification: PKHD1_Ex45F, 5′-CAAACTGT GA AGCTCTGGAA CAGAG-3′, and PKHD1_Ex46R, 5′-GCAAATACTT CAGTTACTGA CAGC-3′. The resulting PCR products were checked on 1 % agarose gels. To obtain smaller PCR products, PCR was performed with the following primers: PKHD1_Intron44, 5′-GCACAGGAAC ATCACCCAAT CTCCAAC-3′, and PKHD1_Intron46-2, 5′-CGGTGCTGTT TACCGTACCC TC-3′. The PCR conditions were 35 cycles of 10 s at 98 °C, 30 s at 60 °C, and 30 s at 72 °C. The PCR products were subjected to ExoSAP-IT digestion (Affymetrix) and then sequenced bidirectionally by capillary electrophoresis (ABI3730 Genetic Analyzer). Breakpoint sequences were characterized using RepeatMasker (http://www.repeatmasker.org/) and non-B DB (https://nonb-abcc.ncifcrf.gov/apps/site/default).

Case presentation

A healthy couple, both 23 years old, consulted our facility after they noticed their fifth pregnancy at 4 weeks of gestation. Their first pregnancy was uncomplicated, and

Table 1 PCR primers used for microsatellite analysis

Marker	Forward primer (FAM)	Backward primer
D6S465	GTCCAGAAGGGAATTTTCTACTCTTTG	CTTTTCAATCATATAACTTTAAAAATGCC
3–204.2 k	GCGTTGACCTATTTCTACACAG	CTTAGGCAAATAAGACCTGGAGAGG
D6S1714	TGTATCCACTGCCATCACTT	AGCACCAAATGACACAGAAC
D6S243	AATAGAACAAATTTGGCCTCTGG	CATCCTTAGAATGAAAAATTACTCAGG
MBC-2 (D6S0919i)	CATGAGGTGAGAGTGAGAAGAGC	AAAGCCAGTTTCCTGACAC
D6S1344	AGCCCTGTGGTTATTTATGCTTCTC	GGTTGTTCCTTCTCTGAACATGGCCC
5–326 k (D6S0460i)	CCTACCCTCTAAAAGGATCTGGG	CCCCACCTACCAACTCTGAATAAA

they had a healthy boy (Fig. 1). The second pregnancy was complicated by oligohydramnios. At 1 week before the due date, the woman vaginally delivered a boy, who died at the second day after birth from respiratory distress due to pulmonary hypoplasia. The woman subsequently got pregnant and the pregnancy was again complicated by oligohydramnios. At 1 month before the due date, the woman delivered a girl via Caesarian section due to breech presentation, who also died at the second day after birth due to respiratory distress. An autopsy was performed and multiple cysts were observed in both the liver and kidneys. The neonate was thus diagnosed with ARPKD. The fourth pregnancy ended in an early pregnancy loss. Soon after they noticed the fifth pregnancy, they consulted our facility to undergo prenatal genetic testing for ARPKD. The couple was screened by abdominal ultrasound and no polycystic kidney disease was observed.

Consent

Written informed consent was obtained from the patient for publication of this manuscript and any accompanying images. A copy of the written consent is available for review by the Editor of this journal.

Results

Carrier testing by target exome sequencing

We performed carrier testing using target exome sequencing of genomic DNA only from both parents because the DNA of the proband obtained from the FFPE sample was too degraded to produce unbiased sequence data. A missense mutation, c.9008C>T (p.S3003F), was identified in exon 58 of the *PKHD1* gene in the paternal genome. Sanger sequencing was performed and the presence of the mutation was confirmed (Fig. 2). The DNA from the FFPE tissue also carried the p.S3003F mutation, whereas the mother and healthy sibling did not. This mutation has not been reported in the human genomic database. The position of the mutated amino acid is at the highly conserved region of the extracellular domain just before the transmembrane domain (phastCons = 0.901, cons score GERP = 5.67). The SIFT score is 0 (deleterious) and PolyPhen 2 score is 0.984 (probably damaging), suggesting a pathogenic mutation. On the other hand, no possible pathogenic mutation was identified in the maternal genome.

Prenatal diagnosis by haplotype analyses

Since a maternal mutation was not identified, we decided to perform prenatal diagnosis by haplotype analysis. We selected seven microsatellite markers encompassing the entire *PKHD1* gene, including upstream and downstream regions (Fig. 3a). By analyses of DNA from the parents, proband, and the healthy sibling, the disease haplotype was successfully determined (Fig. 3b). The healthy sibling was found to be a carrier of the maternal disease haplotype. We then performed an amniocentesis at 17 weeks of gestation. The DNA isolated from amniotic fluid was analyzed for the genotype of these microsatellite markers, and the results of the typing showed that the fetus was a carrier of the maternal disease haplotype but not of the paternal pathogenic haplotype (Fig. 3b). The couple decided to continue the pregnancy and finally obtained a healthy newborn.

Intragenic duplication identified by MLPA

We subsequently reanalyzed the target exome sequencing data, focusing on read depth to identify deletion or

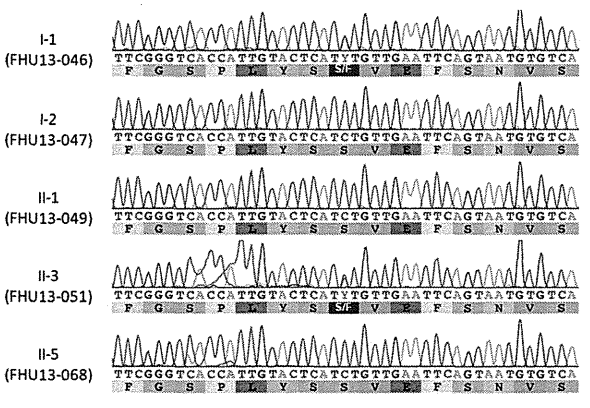

Fig. 2 Pathogenic nucleotide alteration of the *PKHD1* gene identified in the paternal allele. Sample names are indicated on the left: FHU14–046 (I-1, father), FHU13–047 (I-2, mother), FHU13–049 (II-1, healthy sibling), FHU13–051 (II-3, proband), and FHU13–068 (II-5, amniotic fluid)

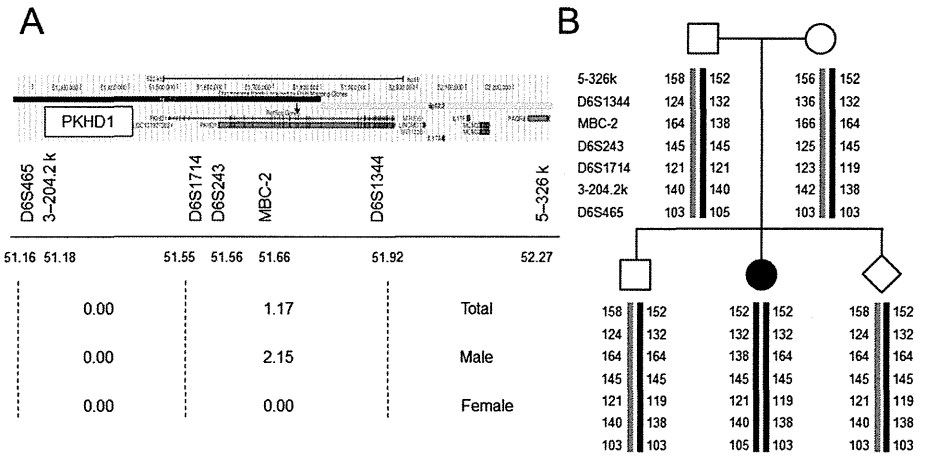

Fig. 3 Microsatellite analysis of the disease haplotype. **a** Genomic structure of the region around the *PKHD1* gene. Seven microsatellite markers were used. The upper panel indicates a transcription map of this region with the name of the seven markers at the bottom. Physical distances (middle panel) as well as genetic distances (lower panel) between the markers are indicated. The location of exons 45 and 46 (arrow) are between MBC-2 and D6S1344. **b** Haplotype analysis of the family members. The numbers indicate the size of the PCR products

duplication mutations in the maternal genome. The CEQer algorithm revealed that the read depths of exons 45 and 46 were higher than those of other exons (Additional file 1: Figure S1). We then performed MLPA for all exons of the *PKHD1* gene using genomic DNA from both parents as well as a normal control. The amounts of PCR products for exons 45 and 46 in maternal DNA were 1.5 times higher than those from the father or normal control (Fig. 4a). A similar finding was also observed in the DNA from the healthy sibling. This duplication is not found in the database of copy number variations. We considered that the maternal mutation was a duplication of exons 45 and 46. If the duplication is a tandem repeat, it results in a frameshift that produces a pathogenic C-terminally truncated protein.

To analyze the breakpoint of this duplication at a nucleotide resolution, we designed inversely oriented PCR primers within both exons 45 and 46. Long-range PCR using primers successfully yielded a PCR product that incorporated the junction of the tandem duplication. Multiple PCR primers were then designed upstream and downstream of the putative breakpoint (introns 44 and 46) and PCR-direct sequencing was performed (Fig. 4b). Sequence analysis of the PCR product revealed the following: rsa[hg19] 6p12.3(51,746,249–51,751,855) × 3. The proximal and distal region was joined with a one-nucleotide microhomology (Fig. 4c).

We further analyzed the sequence around the proximal and distal breakpoint regions. Both of the breakpoints in introns 44 and 46 were located near the LINE1 element, whereas no substantial homology was found between the breakpoint regions (data not shown). We did not identify any non-B DNA motif that could have induced replication fork stalling at either the proximal or distal breakpoint regions [12].

Discussion

In our present study, we used target exome sequencing as a carrier test for the prenatal diagnosis of ARPKD. In ARPKD, genetic screening of the *PKHD1* gene is typically performed by PCR amplification of all coding exons followed by Sanger sequencing. This method is laborious and time-consuming however because the *PKHD1* gene is a large gene spanning a 470-kb genomic region and consisting of 86 exons, including alternatively spliced exons, and recently new exons were identified further [2, 3, 13]. For prenatal diagnosis, each mutation of the carrier parents needs to be determined within a short period. Target exome sequencing can overcome these issues. Because the sequence of all coding exons can be obtained within a week, this strategy would be particularly useful when a carrier couple consults a medical facility for a prenatal diagnosis after they notice their pregnancy.

In ARPKD, genetic screening of the *PKHD1* gene by PCR-direct sequencing of all coding exons can identify disease-causing mutations in up to 82 % of cases [14]. Since most mutations identified by this method are nucleotide alterations, the remaining 18 % might carry copy number mutations that can escape this screening. One report has stated that MLPA screening did not identify any exon deletion/duplication mutation in 39 ARPKD families [5]. Two previous case reports have described multiple exon deletions in the *PKHD1* gene [15, 16]. To our knowledge, our current study is the first report of a duplication mutation in the *PKHD1* gene in a patient with ARPKD. Quantitative analysis of the exome sequence data

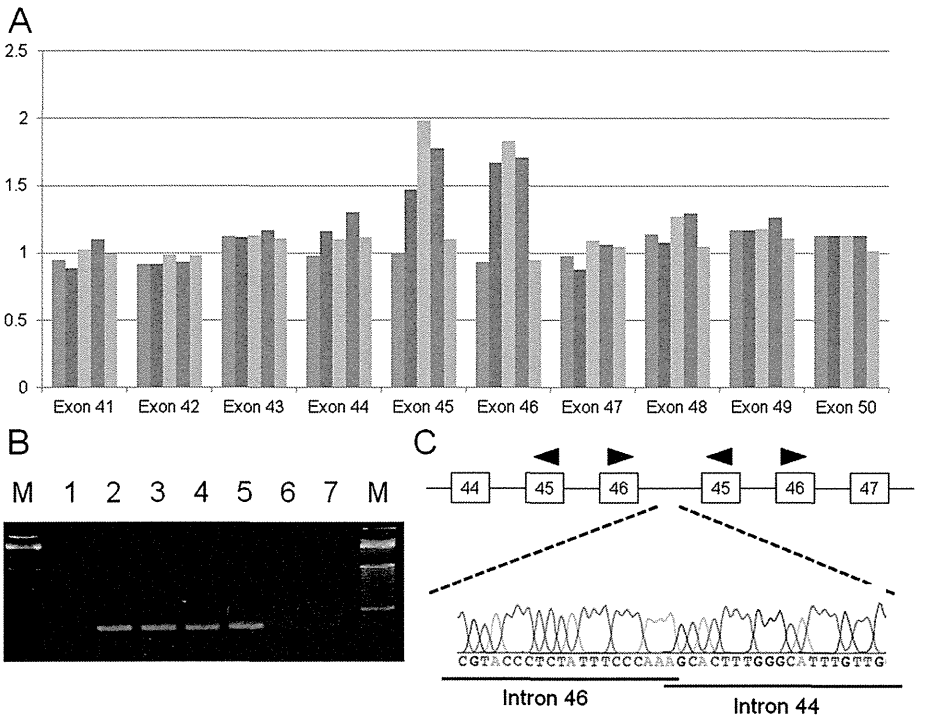

Fig. 4 Exon duplication of the *PKHD1* gene identified in the maternal allele. **a** Diagram of the MLPA results. Dark blue box, FHU14–046 (I-1, father); red box, FHU13–047 (I-2, mother); green box, FHU13–049 (II-1, healthy sibling); purple box, FHU13–068 (II-5, amniotic fluid); light blue box, normal healthy control. **b** Results of junction PCR analysis. Lane M, size markers; lane 1, FHU14–046 (I-1, father); lane 2, FHU14–047 (I-2, mother); lane 3, FHU13–049 (II-1, healthy sibling); lane 4, FHU13–051 (II-3, proband); lane 5, FHU13–068 (II-5, amniotic fluid); lane 6, normal healthy control; lane 7, water control. **c** Results of Sanger sequencing of the junction PCR product. The upper panel indicates the exon-intron structure around the junction

provided a clue to the duplication which was successfully identified by subsequent MLPA. Since target exome analysis may identify a mutation at a nucleotide resolution as well as the copy number variation of the exons, target exome sequencing could replace PCR-direct sequencing or other related PCR-based screening techniques in the near future.

The junction of the duplication showed one-nucleotide identity between the breakpoints without extensive homology, suggesting that fork stalling and template switching or microhomology-mediated breakage-induced replication is a plausible mechanism its formation [17]. Since we found no sequence motif susceptible to the formation of a non-B structure, replication stalling might have occurred in a sequence-independent fashion. It has also been speculated that two introns are located at close proximity in the nucleus at the timing of the replication stall in either of the introns [18].

We identified the duplication junction at a nucleotide resolution, which allowed us to detect the pathogenic allele by simple PCR. In our current case, the duplication mutation was identified after the delivery of the healthy newborn. However, if careful examination of exome data had enabled the identification of both the paternal mutation and maternal duplication, we could have performed prenatal diagnosis directly by detection of both paternal and maternal mutations. In the case of an amniocentesis, the sample often contains a considerable amount of dead cells that impede copy number analysis techniques such as cytogenetic microarray and MLPA. The determination of the breakpoint would provide a simple PCR-based diagnosis of the pathogenic allele. We thus conclude that target exome sequencing of the *PKHD1* gene has utility as a carrier test for the prenatal diagnosis of ARPKD.

Conclusion

This case suggests the potential usefulness of target exome sequencing in the prenatal diagnosis of the *PKHD1* gene in ARPKD. This is the first report of intragenic duplication in the *PKHD1* gene in ARPKD.

Additional file

Additional file 1: Figure S1. *Quantitative analysis of the exome data using the Comparative Exome Quantification analyzer (CEQer). The upper panel indicates the map of the PKHD1 gene. The lower panel indicates the normalized read depth.* (TIFF 93 kb)

Abbreviations

ARPKD: Autosomal recessive polycystic kidney disease; FFPE: Formalin-fixed, paraffin-embedded; MLPA: Multiplex ligation-dependent probe amplification.

Competing interests
The authors declare that they have no competing interests.

Authors' contributions
Jun Miyazaki has made substantial contributions to conception and design, or acquisition of data, or analysis and interpretation of data. Mayuko Ito has made substantial contributions to conception and design, or acquisition of data, or analysis and interpretation of data. Haruki Nishizawa has made substantial contributions to conception and design, or acquisition of data, or analysis and interpretation of data and has been involved in drafting the manuscript or revising it critically for important intellectual content. Takema Kato has made substantial contributions to conception and design, or acquisition of data, or analysis and interpretation of data. Yukito Minami has made substantial contributions to conception and design, or acquisition of data, or analysis and interpretation of data. Hidehito Inagaki has made substantial contributions to conception and design, or acquisition of data, or analysis and interpretation of data. Tamae Ohye has made substantial contributions to conception and design, or acquisition of data, or analysis and interpretation of data. Masafumi Miyata has made substantial contributions to conception and design, or acquisition of data, or analysis and interpretation of data. Hiroko Boda has made substantial contributions to conception and design, or acquisition of data, or analysis and interpretation of data. Yuka Kiriyama has made substantial contributions to conception and design, or acquisition of data, or analysis and interpretation of data. Makoto Kuroda has made substantial contributions to conception and design, or acquisition of data, or analysis and interpretation of data. Takao Sekiya has made substantial contributions to conception and design, or acquisition of data, or analysis and interpretation of data. Hiroki Kurahashi has been involved in drafting the manuscript or revising it critically for important intellectual content, has given final approval of the version to be published, and agrees to be accountable for all aspects of the work in ensuring that questions related to the accuracy or integrity of any part of the work are appropriately investigated and resolved. Takuma Fujii has been involved in drafting the manuscript or revising it critically for important intellectual content. All authors read and approved the final manuscript.

Acknowledgments
The authors thank Dr. Makiko Tsutsumi for helpful discussions and Mrs. Narumi Kamiya for technical assistance. These studies were supported by a Grant-in-Aid for Scientific Research from the Ministry of Education, Culture, Sports, Science, and Technology of Japan (H.K), and grants for Research on Intractable Diseases from the Ministry of Health, Labour and Welfare of Japan (H.K).

Author details
[1]Division of Molecular Genetics, Institute for Comprehensive Medical Science, Fujita Health University, 1-98 Dengakugakubo, Kutsukake-cho, Toyoake, Aichi 470-1192, Japan. [2]Department of Obstetrics and Gynecology, Fujita Health University School of Medicine, 1-98 Dengakugakubo, Kutsukake-cho, Toyoake, Aichi 470-1192, Japan. [3]Genome and Transcriptome Analysis Center, Fujita Health University, Aichi, Japan. [4]Department of Genetic Counseling, Fujita Health University Hospital, Aichi, Japan. [5]Department of Pediatrics, Fujita Health University School of Medicine, 1-98 Dengakugakubo, Kutsukake-cho, Toyoake, Aichi 470-1192, Japan. [6]Department of Diagnostic Pathology, Fujita Health University School of Medicine, 1-98 Dengakugakubo, Kutsukake-cho, Toyoake, Aichi 470-1192, Japan.

Received: 4 January 2015 Accepted: 12 October 2015
Published online: 26 October 2015

References

1. Zerres K, Rudnik-Schöneborn S, Deget F, Holtkamp U, Brodehl J, Geisert J, et al. Autosomal recessive polycystic kidney disease in 115 children: clinical presentation, course and influence of gender. Acta Paediatr. 1996;85:437–45.
2. Ward CJ, Hogan MC, Rossetti S, Walker D, Sneddon T, Wang X, et al. The gene mutated in autosomal recessive polycystic kidney disease encodes a large, receptor-like protein. Nat Genet. 2002;30:259–69.
3. Onuchic LF, Furu L, Nagasawa Y, Hou X, Eggermann T, Ren Z, et al. PKHD1, the polycystic kidney and hepatic disease 1 gene, encodes a novel large protein containing multiple immunoglobulin-like plexin-transcription-factor domains and parallel beta-helix 1 repeats. Am J Hum Genet. 2002;70:1305–17.
4. Sharma N, Berbari NF, Yoder BK. Ciliary dysfunction in developmental abnormalities and diseases. Curr Top Dev Biol. 2008;85:371–427.
5. Losekoot M, Haarloo C, Ruivenkamp C, White SJ, Breuning MH, Peters DJ. Analysis of missense variants in the PKHD1-gene in patients with autosomal recessive polycystic kidney disease (ARPKD). Hum Genet. 2005;118:185–206.
6. Rossetti S, Torra R, Coto E, Consugar M, Kubly V, Málaga S, et al. A complete mutation screen of PKHD1 in autosomal-recessive polycystic kidney disease (ARPKD) pedigrees. Kidney Int. 2003;64:391–403.
7. Bergmann C, Senderek J, Küpper F, Schneider F, Dornia C, Windelen E, et al. PKHD1 mutations in autosomal recessive polycystic kidney disease (ARPKD). Hum Mutat. 2004;23:453–63.
8. Zhang D, Lu L, Yang HB, Li M, Sun H, Zeng ZP, et al. Exome sequencing identifies compound heterozygous PKHD1 mutations as a cause of autosomal recessive polycystic kidney disease. Chin Med J. 2012;125:2482–6.
9. Piazza R, Magistroni V, Pirola A, Redaelli S, Spinelli R, Redaelli S, et al. CEQer: a graphical tool for copy number and allelic imbalance detection from whole-exome sequencing data. PLoS One. 2013;8, e74825.
10. Consugar MB, Anderson SA, Rossetti S, Pankratz VS, Ward CJ, Torra R, et al. Haplotype analysis improves molecular diagnostics of autosomal recessive polycystic kidney disease. Am J Kidney Dis. 2005;45:77–87.
11. Lau EC, Janson MM, Roesler MR, Avner ED, Strawn EY, Bick DP. Birth of a healthy infant following preimplantation PKHD1 haplotyping for autosomal recessive polycystic kidney disease using multiple displacement amplification. J Assist Reprod Genet. 2010;27:397–407.
12. Cer RZ, Donohue DE, Mudunuri US, Temiz NA, Loss MA, Starner NJ, et al. Non-B DB v2.0: a database of predicted non-B DNA-forming motifs and its associated tools. Nucleic Acids Res. 2013;41:D94–100.
13. Boddu R, Yang C, O'Connor AK, Hendrickson RC, Boone B, Cui X, et al. Intragenic motifs regulate the transcriptional complexity of Pkhd1/PKHD1. J Mol Med (Berl). 2014;92:1045–56.
14. Gunay-Aygun M, Tuchman M, Font-Montgomery E, Lukose L, Edwards H, Garcia A, et al. PKHD1 sequence variations in 78 children and adults with autosomal recessive polycystic kidney disease and congenital hepatic fibrosis. Mol Genet Metab. 2010;99:160–73.
15. Bergmann C, Küpper F, Schmitt CP, Vester U, Neuhaus TJ, Senderek J, et al. Multi-exon deletions of the PKHD1 gene cause autosomal recessive polycystic kidney disease (ARPKD). J Med Genet. 2005;42, e63.
16. Zvereff V, Yao S, Ramsey J, Mikhail FM, Vijzelaar R, Messiaen L. Identification of PKHD1 multiexon deletions using multiplex ligation-dependent probe amplification and quantitative polymerase chain reaction. Genet Test Mol Biomarkers. 2010;14:505–10.
17. Hastings PJ, Lupski JR, Rosenberg SM, Ira G. Mechanisms of change in gene copy number. Nat Rev Genet. 2009;10:551–64.
18. De S, Michor F. DNA replication timing and long-range DNA interactions predict mutational landscapes of cancer genomes. Nat Biotechnol. 2011;29:1103–8.

Journal of Virological Methods 228 (2016) 74–78

Contents lists available at ScienceDirect

Journal of Virological Methods

journal homepage: www.elsevier.com/locate/jviromet

A simple cytogenetic method to detect chromosomally integrated human herpesvirus-6

Tamae Ohye[a,b], Yoshiki Kawamura[c], Hidehito Inagaki[a], Akiko Yoshikawa[c], Masaru Ihira[d], Tetsushi Yoshikawa[c], Hiroki Kurahashi[a,*]

[a] Division of Molecular Genetics, Institute for Comprehensive Medical Science, Fujita Health University, Toyoake, Aichi 470-1192, Japan
[b] Department of Clinical Hematology, Faculty of Medical Technology, Fujita Health University, Toyoake, Aichi 470-1192, Japan
[c] Department of Pediatrics, Fujita Health University School of Medicine, Toyoake, Aichi 470-1192, Japan
[d] Faculty of Clinical Engineering, Fujita Health University School of Health Sciences, Toyoake, Aichi 470-1192, Japan

Article history:
Received 28 April 2015
Received in revised form 2 November 2015
Accepted 3 November 2015
Available online 6 November 2015

Keywords:
Chromosomally integrated human herpesvirus-6
FISH
PCR-based method
HHV-6 probe
Chromosome
Telomere

ABSTRACT

Some healthy individuals carry human herpesvirus-6 (HHV-6) within a host chromosome, which is called inherited chromosomally integrated human herpesvirus-6 (iciHHV-6). Because iciHHV-6 is generally considered a non-pathogenic condition, it is important to distinguish iciHHV-6 from HHV-6 reactivation in immunocompromised hosts because both conditions manifest high copy numbers of the HHV-6 in peripheral blood mononuclear cells. Although fluorescent *in situ* hybridization (FISH) is a reliable method for the diagnosis of iciHHV-6, HHV-6-specific FISH probes are not commercially available. In our present study, we established a simple PCR-based method for producing FISH probes that can detect the chromosomal integration site of iciHHV-6 at high sensitivity. Using these probes, we confirmed that HHV-6 signals were consistently located at the telomeric region in all of the 13 iciHHV-6 individuals examined. Interestingly, in all seven Japanese iciHHV-6A patients, signals were detected exclusively on chromosome 22q. This method provides a simple and fast approach for iciHHV-6 diagnosis in the clinical laboratory.

1. Introduction

Human herpesvirus 6 (HHV-6) includes HHV-6A and HHV-6B, which are two closely related herpesvirus species with an overall nucleotide sequence identity of 90% (Abtashi et al., 1993; Dominguez et al., 1999; Isegawa et al., 1999). Primary HHV-6B infection occurs in infancy and causes exanthem subitum, a common febrile exanthematous disease (Yamanishi et al., 1988; Yoshikawa et al., 1989). In contrast, the clinical features of primary HHV-6A infection and the diseases directly associated with it remain to be identified. Following primary infection, HHV-6 remains latent in monocytes and macrophages and persists in the salivary glands (Fox et al., 1990; Kondo et al., 1991). Immune suppression in transplant recipients induces HHV-6B reactivation, with serious clinical effects, such as pneumonitis, encephalitis, and bone marrow suppression (Yoshikawa, 2004; Yoshikawa et al., 1991).

Some normal healthy individuals carry the HHV-6 genome within a host chromosome, which is known as inherited chromosomally integrated herpesvirus-6 (iciHHV-6) (Hall et al., 2008; Morissette and Flamand, 2010). The presence of iciHHV-6 within the human genome is not uncommon, with a reported incidence of 1% and 0.21% in healthy Caucasian and Japanese populations, respectively (Hall et al., 2008; Pellett et al., 2011; Tanaka-Taya et al., 2004). The integration of the viral genome occurs in a homology-dependent manner between human telomere repeat sequences and viral telomere repeat-like sequences (TRSs), and the integrated viral genome is transmitted by Mendelian inheritance (Arbuckle et al., 2010, 2013; Ohye et al., 2014). iciHHV-6 carriers are often identified as high-titer virus carriers during screenings for HHV-6 reactivation in immunocompromised hosts.

It is important to distinguish iciHHV-6 from HHV-6 reactivation in immunocompromised hosts. Although both conditions manifest a high copy number of HHV-6 in peripheral blood mononuclear cells, fluorescent *in situ* hybridization (FISH) is a reliable method for diagnosis of iciHHV-6. FISH requires clones with a long insert, such as bacterial artificial chromosomes (BACs) or cosmid clones, as specific probes. However, such clones are often unstable and lose inserts during bacterial culture because of direct repeat structures within the long inserts. For diagnosis of iciHHV-6, FISH requires

* Corresponding author at: Division of Molecular Genetics, Institute for Comprehensive Medical Science, Fujita Health University, 1-98 Dengakugakubo, Kutsukake-cho, Toyoake, Aichi 470-1192, Japan.
E-mail address: kura@fujita-hu.ac.jp (H. Kurahashi).

http://dx.doi.org/10.1016/j.jviromet.2015.11.001
0166-0934/

large DNA fragments derived from HHV-6 genome as probes. However, HHV-6-specific FISH probes are not commercially available. A plasmid bearing the largest *PstI* restriction fragment of 15.3 kb has been conventionally used (Tanaka-Taya et al., 2004) but this plasmid is not easy to handle due to the instability of the large insert, as expected.

In our present study, we established a simple PCR-based method for producing FISH probes that can detect the chromosomal integration site harboring iciHHV-6 at high sensitivity. Using these probes, we examined the integration sites of 13 Japanese individuals harboring iciHHV-6A or -6B.

2. Materials and methods

2.1. Human subjects

We analyzed 13 Japanese cases that were suspected to have iciHHV-6A or -6B by having a genome equivalent copy number of viral DNA in peripheral blood samples estimated by qPCR (Tanaka et al., 2000). The primers used for the qPCR are as follows: H6TA1, TTTGCAGTCATCACGATCGG; H6TA2, AGAGCGACAAATTGGAGGTTTC; probe, AAGCCACAGCAGCCA. These primer set can amplify both iciHHV-6A and -6B genomes. Determination of iciHHV-6A or -6B was performed by analysis of the restriction fragment lengths of the PCR products designed within the U31 gene (Ablashi et al., 1991). All of the six iciHHV-6B cases were reported previously (Ohye et al., 2014). The additional seven iciHHV-6A cases were included in this study. The triggers for the diagnoses of the iciHHV-6A cases are listed in Table 1. After informed consent was obtained, peripheral blood samples were obtained again from each patient for cytogenetic analyses. Our study was approved by the Ethical Review Board for Human Genome Studies of Fujita Health University (accession number 90, approved on 24 March 2010).

2.2. Preparation of viral probes using long-range PCR

PCR primers were designed based on HHV-6B sequences (Table 2). Long-range PCR was performed with LA Taq (Takara, Japan). The PCR conditions were as follows: 98 °C for 2.5 min, 35 cycles at 98 °C for 10 s and 60 °C for 10 min, followed by a final extension at 60 °C for 10 min. Genomic DNA of HHV-6B isolated from the Z29 strain was used as the PCR template. A plasmid, pSTY01, bearing the largest *PstI* restriction fragment of HHV-6B (15.3 kb) was also used as a probe (Fig. 1) (Isegawa et al., 1999; Tanaka-Taya et al., 2004).

Viral DNA was prepared from the virus-infected cord blood mononuclear cells, digested with *Eco*RI and blotted onto a nylon membrane. The mixture of the PCR products was labeled with α-^{32}P-dCTP by random primer method. Southern Hybridization and detection was performed by standard methods.

2.3. Fluorescent in situ hybridization

FISH was performed using a standard method. Briefly, phytohemagglutinin (PHA)-stimulated lymphocytes or Epstein–Barr virus (EBV)-transformed lymphoblasts were arrested by treatment with colcemid. Metaphase preparations were obtained by hypotonic treatment using 0.075 M KCl followed by methanol/acetate fixation. Probes, plasmids, or a mixture of the PCR products, were labeled by nick-translation with biotin-16-dUTP or digoxigenin-11-dUTP. The metaphase chromosomes on the slides were denatured in 70% formamide/2× saline sodium citrate buffer (SSC) at 73 °C for 4 min, immersed in 70% ethanol at −20 °C for 2 min, and dehydrated in a 100% ethanol. A mixture of probe solutions was denatured at 70 °C for 10 min, chilled on ice for 5 min, and mixed with an equal volume of 4× SSC containing 20% dextran sulfate. The final hybridization mixture was applied to denatured slides. The slides were covered with cover glass and incubated in a humid box at 37 °C for 18 h. After hybridization, excess probes were washed in 50% formamide/2× SSC at 37 °C for 10 min, 2× SSC, 1× SSC, and 4× SSC at room temperature for 10 min each. The probes were detected using either Alexa Fluor® 488-conjugated streptavidin or rhodamine-conjugated anti-digoxigenin, respectively. The detection was performed in 4× SSC with 1% blocking reagent in a humid box at 37 °C for 45 min, and then the slide was washed with 4× SSC, 4× SSC with 0.05% Triton X, 4× SSC, and then 2× SSC at room temperature for 10 min each. Chromosomes were visualized by counter-staining with 4′,6-diamino-2-phenylindole (DAPI). As reference standards, we used the following chromosome-specific probes: Human Chromosome 14/22, Biotin Labeled (CPBR-70-014C, Cambio, Cambridge, UK), TelVysion 6p SpectrumGreen (5J03-06, Abbott Molecular, Illinois, USA), and TelVysion Xq/Yq SpectrumOrange (5J04-23, Abbott Molecular, Illinois, USA). To prepare telomere-specific probes, we performed PCR using the Tel-A primer, 5′-CCCTAACCCTAACCCTAACCCTAACC-3′ (Ohye et al., 2014).

3. Results

The HHV-6 genome comprises a linear double-stranded DNA of ~162 kb flanked by identical 8 kb direct repeats at the left and right ends (DR-L and DR-R). The ~145 kb central region is called the unique long region (UL) and includes 97 coding genes (De Bolle et al., 2005; Gompels and Macaulay, 1995). We designed five PCR

Table 1
Triggers for the diagnoses and the chromosome locations of iciHHV-6 in the study population.

Family	Case	Type	Chromosome	Triggers for the diagnosis of iciHHV-6
1	26	A	22q	Monitoring after cord blood transplantation
	29	A	22q	Father of Case 26
2	37	A	22q	Monitoring after cord blood transplantation
3	45	A	22q	Monitoring after bone marrow transplantation
4	66	A	22q	Uveitis
5	9	A	22q	Differential diagnosis of encephalitis
6	15	A	22q	Multiform exudative erythema
7	18	B	22q	Monitoring after bone marrow transplantation Aplastic anemia
8	19	B	22q	Differential diagnosis of mycoplasma Encephalitis
	20	B	22q	Mother of Case 19
9	28	B	Xp	Monitoring after bone marrow transplantation Congenital pure red cell aplasia
10	31	B	6q	Differential diagnosis of febrile skin rash
11	63	B	Xp	Uveitis

Table 2
Primer sequences for the PCR products used as FISH probes.

PCR product name	Forward primer	Reverse primer	PCR product size (kb)
U11-18	5′-GCGTGGTTACAATTTGAGACATAGC-3′	5′-GAAACTTGGAGCTATATGCATCTCTAC-3′	8.5
U18-25	5′-AATGTTCAAAGTGCCATTGGCATCTG-3′	5′-GTAGTAGTGTTTGACGGCCACG-3′	7.3
U38-40	5′-CATTACCTCTGCAATAGCAGAAAACG-3′	5′-TCTCTGTGTGTGTTGTGCGCTAG-3′	7.6
U43-47	5′-GCGATGGAACAATGTACTTGTTTGC-3′	5′-TCACCCGACATGCTTCACATCTC-3′	7.1
U72-76	5′-GTGTTATTCGTTTTCATCCATTAGGC-3′	5′-CACAGAGCATCAGCAAATTCGCTG-3′	8.0

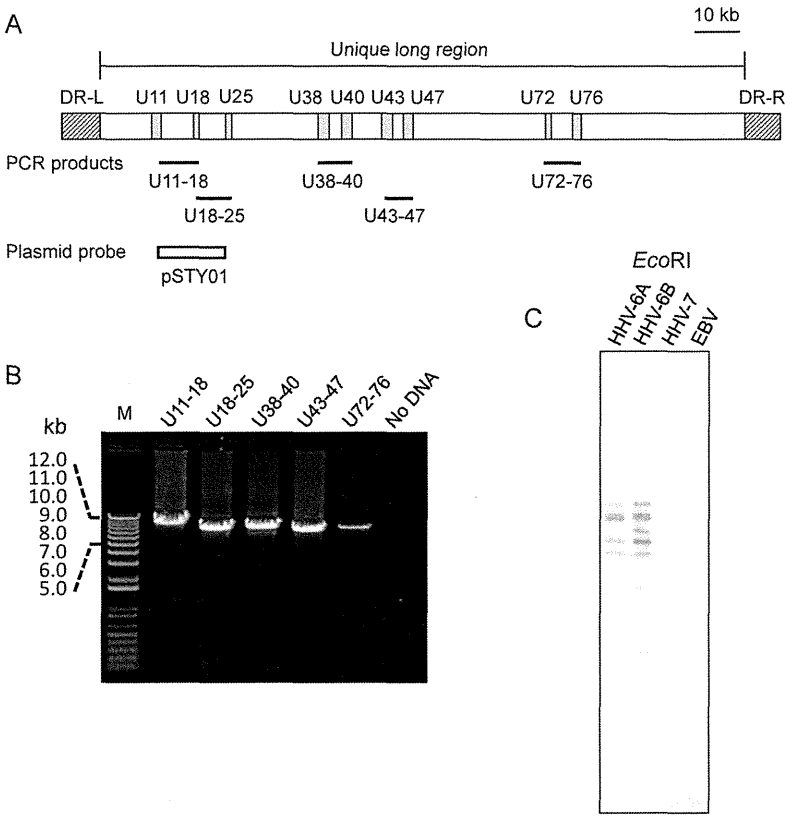

Fig. 1. Generation of PCR-based FISH probes for detection of HHV-6. (A) Schematic representation of the HHV-6 genome. Gray boxes indicate coding genes, whereas hatched boxes indicate DRs. The positions of the PCR probes are indicated below the diagram. The position of the plasmid probe is also depicted. (B) Agarose gel electrophoresis for PCR probes. Lane 1, U11-18; lane 2, U18-25; lane 3, U38-40; lane 4, U43-47; lane 5, U72-76; and lane 6, no DNA. (C) Evaluating of the HHV-6-specificity by Southern hybridization. *Eco*RI-digested viral DNA was subjected to hybridization with the mixture of PCR probes. Lane 1, U1102 (HHV-6A); lane 2, Z29 (HHV-6B); lane 3, HHV-7; and lane 4, EBV.

systems within the UL of the HHV-6B that could yield PCR products ranging from 7.1 to 8.5 kb in size (Fig. 1A, Table 2). The PCR primers were designed at the coding region to avoid the effects of sequence variations among strains. All of the PCR primer pairs yielded specific PCR products in viral genomic DNA isolated from the Z29 strain (Fig. 1B). To evaluate the specificity of the probes, we performed Southern hybridization using the PCR probes, resulting in signals only in the HHV-6A and HHV-6B DNA, not in HHV-7 and EBV (Fig. 1C). A probe cocktail consisting of equal amounts of these PCR products was used for the subsequent FISH procedure.

Thirteen cases that were suspected to have iciHHV-6A or -6B estimated by qPCR were analyzed. Six cases were found to carry HHV-6B, whereas seven cases had iciHHV-6A. In our previous study, FISH analysis with a plasmid probe bearing HHV-6 genomic DNA (pSTY01) detected virus-specific signals in these six iciHHV-6B cases (Ohye et al., 2014). The integration sites were on the long arm of chromosome 22 in three cases, on the long arm of chromosome 6 in one case, and on the short arm of chromosome X in two cases (Table 1). In these cases, we successfully detected FISH signals for HHV-6B with the PCR probes in the same chromosomal region. Both PHA-stimulated and EBV-transformed lymphoblasts showed similar signals. Signals were comparable to or even stronger than those obtained using standard FISH probes produced from plasmid clones (Fig. 2). HHV-6 signals were consistently detected at the end of the chromosomes in all six cases, presumably at the telomeric regions, as reported previously (Ohye et al., 2014). Indeed, the HHV-6 signals and the signals of the telomere probes were co-localized at the end of chromosomes (Fig. 2, inset). In contrast, no signal was detected on the metaphase from normal individuals (Supplementary Fig. 1).

Supplementary material related to this article can be found, in the online version, at http://dx.doi.org/10.1016/j.jviromet.2015.11.001.

In the seven iciHHV-6A cases, we also detected robust FISH signals with the PCR probes generated from HHV-6B (Fig. 2). We could make a definitive diagnosis of either iciHHV-6A or -6B by FISH with our PCR probe cocktail, although we could not distinguish between the iciHHV-6A and -6B. The FISH signals were detectable only on one of the homologues, suggesting that all seven individuals were heterozygotes for iciHHV-6A. Interestingly, the HHV-6 signals were exclusively detected on chromosome 22 in all seven iciHHV-6A patients, even in the unrelated cases (Table 1). Similar

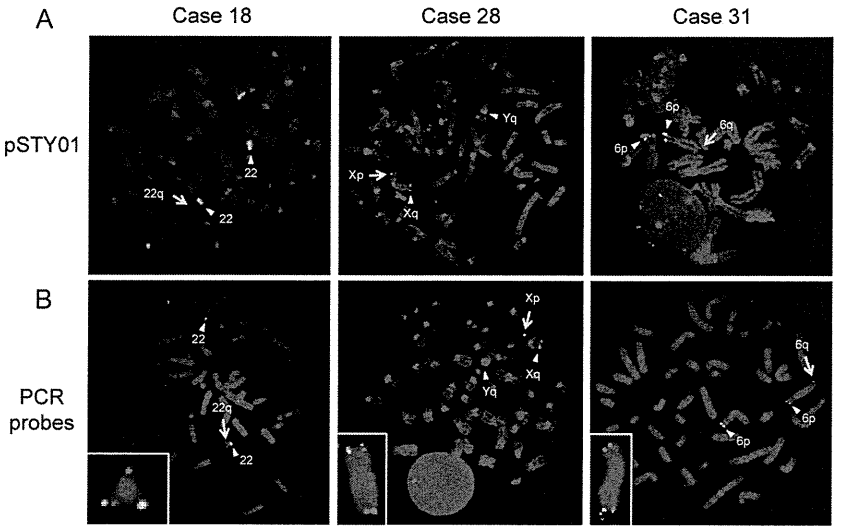

Fig. 2. Characterization of iciHHV-6B by FISH. FISH analyses of metaphase chromosomes derived from the iciHHV-6B study subjects. Signals from the pSTY01 plasmid (A) and PCR (B) probes are detectable at the end of chromosome 22q (case 18), chromosome 6q (case 31), and chromosome Xp (case 28) (yellow arrows). The reference signals for the chromosome 14/22 centromere, 6p, and Xq are indicated by the white arrowheads. The PCR probes (green) were also co-hybridized with telomere-specific probes (red) (B, insets). (For interpretation of the references to color in this figure legend, the reader is referred to the web version of this article.)

to iciHHV-6B, the HHV-6 signals were consistently detected at the end of the chromosomes, presumably at the telomeric regions, in all seven cases.

4. Discussion

In our present study, we detected the chromosomally integrated HHV-6 genome in seven carriers of HHV-6A and six carriers of HHV-6B using a PCR-based probe cocktail. FISH probes for the detection of HHV-6 have generally been generated using a plasmid harboring a viral genomic fragment as an insert, but with a suboptimal sensitivity. To increase this sensitivity, plasmid probe cocktails have occasionally been used (Nacheva et al., 2008). Our current PCR-based method is a simple approach that can be performed using standard laboratory equipment. Although the probes were amplified from the HHV-6B genome, the integrated HHV-6 was detected successfully in all patients with iciHHV-6A. This PCR-based method provides an easy and fast way for iciHHV-6 diagnosis in the clinical laboratory.

It is important to distinguish iciHHV-6 from HHV-6 reactivation in immunocompromised hosts. Importance of the diagnosis is also highlighted by the recent finding that the iciHHV is risk factor for the development of angina (Gravel et al., 2015). FISH is a reliable method for the diagnosis of iciHHV-6, but the unavailability of FISH probes has hindered the utility of this method in clinical laboratories. In most laboratories, iciHHV-6 is suspected by the detection of a high copy number of HHV-6 in peripheral blood mononuclear cells and confirmed by one viral copy per cell using real-time PCR (Leong et al., 2007). Recently, the droplet digital PCR assay is used for measurement of the correct copy number of the HHV genome (Sedlak et al., 2014). Although simple qualitative or quantitative PCR for whole blood test is also available, quantitative analysis cannot distinguish between reactivation and iciHHV-6, if the copy number of the virus in the reactivation is near the host genome equivalent (Caserta et al., 2010; Geraudie et al., 2012). We here describe a simple and reliable method for performing the FISH procedure in clinical laboratories. PCR using DNA from nail clipping or hair follicle as a template can be also useful for diagnosis of the iciHHV-6 (Hubacek et al., 2009; Ward et al., 2006). In addition to the diagnosis of iciHHV-6, the FISH method can also provide information on the locus of the integrated chromosome, which cannot be obtained by real-time PCR.

All of the integrated HHV-6 genomes in our current patient series were detected in a telomeric region, regardless of the type of the virus. It has been speculated in previous molecular studies that the HHV-6 viral genome is integrated into human telomeres through a homology-based mechanism that is specific to HHV-6 (Arbuckle et al., 2010, 2013; Ohye et al., 2014). The HHV-6 genome comprises a linear double-stranded DNA of ~162 kb flanked by identical 8 kb direct repeats at the left and right ends (DR-L and DR-R). Each DR contains two TRSs near both ends of the DRs (Gompels and Macaulay, 1995; Thomson et al., 1994). A homology-directed DNA damage response between human telomere repeats and viral TRS is considered to be the mechanism that leads to viral integration. Recently, integration of the virus into the chromosome arm was reported, although no metaphase FISH data was reported (Goel et al., 2013). Detailed characterization of this uncommon case would further elucidate the integration mechanism.

Interestingly, although the integration sites of HHV-6B were found to vary among individual cases, the integration sites of HHV-6A were exclusively the chromosomal end of 22q in all seven iciHHV-6A cases. There is no other report describing integration sites for Japanese iciHHV-6A, although reports for Japanese iciHHV-6B showed the integration at the end of chromosome 22q (Dominguez et al., 1999; Tanaka-Taya et al., 2004). One possible explanation is that the viral integration was a single event that occurred in the past and that all of the iciHHV-6A in the Japanese population was transmitted from a single ancestor. The integration of HHV-6 into the telomeric region is unlikely to change the expression of the important genes in the host genome. Approximately 1% of normal healthy individuals in the general population carry iciHHV-6 chromosomes, although a recent study suggests the possibility of pathogenicity by viral reactivation of the integrated virus (Arbuckle et al., 2010; Endo et al., 2014; Hall et al., 2008). Thus, iciHHV-6 could be transmitted stably to offspring and expand in the general population. In fact, in iciHHV-6A cases of other ethnic origins, integrations into other chromosomes have been reported (Arbuckle et al., 2010; Nacheva et al., 2008). Another possibility is that these HHV-6A integrations are multiple independent events, and that they recurrently occurred at the end of 22q in the Japanese population. Because the subtelomeric region is highly polymorphic, a certain variant of the 22q subtelomere in the Japanese population may have susceptibility to HHV-6 genome

integration (Linardopoulou et al., 2005). Further work is required to characterize the viral integration sites on 22q in each iciHHV-6A case.

In conclusion, we established a simple PCR-based method for producing FISH probes that can detect the chromosomal integration site of iciHHV-6 at high sensitivity. This method provides a simple and fast approach for iciHHV-6 diagnosis in the clinical laboratory.

Conflict of interest statement

The authors declare no conflicts of interest.

Acknowledgments

The authors thank Drs. Koji Kato, Junko Oikawa, Hiroshi Yagasaki, Takahiro Niizuma, Yoshiyuki Takahashi, Seiji Kojima, Takuya Maeda, Tadanobu Yoshikawa, Naomi Kubota, Hisashi Yamamoto, and Akifumi Endo for providing samples, Drs. Makiko Tsutsumi and Takema Kato for helpful discussions, and Junko Kato, Noriko Hayashizono, and Narumi Kamiya for technical assistance. This work was supported by a grant-in-aid for Scientific Research from the Ministry of Education, Culture, Sports, Science, and Technology of Japan, and from the Ministry of Health, Labour and Welfare of Japan, to H.K.

References

Ablashi, D.V., Balachandran, N., Josephs, S.F., Hung, C.L., Krueger, G.R., Kramarsky, B., Salahuddin, S.Z., Gallo, R.C., 1991. Genomic polymorphism, growth properties, and immunologic variations in human herpesvirus-6 isolates. Virology 184, 545–552.

Abtashi, D.V., Agut, H., Berneman, Z., Campadelli-Fiume, G., Carrigan, D., Ceccerini-Nellis, L., Chandran, B., Chou, S., Collandres, H., Cone, R., Dambaugh, T.R., De-whurst, S., DiLuca, D., Foa-Tomasi, L., Fleckenstein, B., Frenke, N., Gallo, R., Gompels, U.A., Hall, C.B., Jones, M., Lawrencew, G., Martin, M., Montagniera, L., Neipe, F., Nicholas, J., Pellett, P.E., Razzaque, A., Torrelli, G., Thomson, B.J., Salahuddin, S., Wyatt, L., Yamanishi, K., 1993. Human herpesvirus-6 strain groups: a nomenclature. Arch. Virol. 129, 363–366.

Arbuckle, J.H., Medveczky, M.M., Luka, J., Hadley, S.H., Luegmayr, A., Ablashi, D., Lund, T.C., Tolar, J., De Meirleir, K., Montoya, J.G., Komaroff, A.L., Ambros, P.F., Medveczky, P.G., 2010. The latent human herpesvirus-6A genome specifically integrates in telomeres of human chromosomes in vivo and in vitro. Proc. Natl. Acad. Sci. U. S. A. 107, 5563–5568.

Arbuckle, J.H., Pantry, S.N., Medveczky, M.M., Prichett, J., Loomis, K.S., Ablashi, D., Medveczky, P.G., 2013. Mapping the telomere integrated genome of human herpesvirus 6A and 6B. Virology 442, 3–11.

Caserta, M.T., Hall, C.B., Schnabel, K., Lofthus, G., Marino, A., Shelley, L., Yoo, C., Carnahan, J., Anderson, L., Wang, H., 2010. Diagnostic assays for active infection with human herpesvirus 6 (HHV-6). J. Clin. Virol. 48, 55–57.

De Bolle, L., Naesens, L., De Clercq, E., 2005. Update on human herpesvirus 6 biology, clinical features, and therapy. Clin. Microbiol. Rev. 18, 217–245.

Dominguez, G., Dambaugh, T.R., Stamey, F.R., Dewhurst, S., Inoue, N., Pellett, P.E., 1999. Human herpesvirus 6B genome sequence: coding content and comparison with human herpesvirus 6A. J. Virol. 73, 8040–8052.

Endo, A., Watanabe, K., Ohye, T., Suzuki, K., Matsubara, T., Shimizu, N., Kurahashi, H., Yoshikawa, T., Katano, H., Inoue, N., Imai, K., Takagi, M., Morio, T., Mizutani, S., 2014. Molecular and virological evidence of viral activation from chromosomally integrated human herpesvirus 6A in a patient with X-linked severe combined immunodeficiency. Clin. Infect. Dis. 59, 545–548.

Fox, J.D., Briggs, M., Ward, P.A., Tedder, R.S., 1990. Human herpesvirus 6 in salivary glands. Lancet 336, 590–593.

Geraudie, B., Charrier, M., Bonnafous, P., Heurte, D., Desmonet, M., Bartoletti, M.A., Penasse, C., Agut, H., Gautheret-Dejean, A., 2012. Quantitation of human herpesvirus-6A, -6B and -7 DNAs in whole blood, mononuclear and polymorphonuclear cell fractions from healthy blood donors. J. Clin. Virol. 53, 151–155.

Goel, P., Tailor, P., Chande, A.G., Basu, A., Mukhopadhyaya, R., 2013. An infectious HHV-6B isolate from a healthy adult with chromosomally integrated virus and a reporter based relative viral titer assay. Virus Res. 173, 280–285.

Gompels, U.A., Macaulay, H.A., 1995. Characterization of human telomeric repeat sequences from human herpesvirus 6 and relationship to replication. J. Gen. Virol. 76 (Pt 2), 451–458.

Gravel, A., Dubuc, I., Morissette, G., Sedlak, R.H., Jerome, K.R., Flamand, L., 2015. Inherited chromosomally integrated human herpesvirus 6 as a predisposing risk factor for the development of angina pectoris. Proc. Natl. Acad. Sci. U. S. A. 112, 8058–8063.

Hall, C.B., Caserta, M.T., Schnabel, K., Shelley, L.M., Marino, A.S., Carnahan, J.A., Yoo, C., Lofthus, G.K., McDermott, M.P., 2008. Chromosomal integration of human herpesvirus 6 is the major mode of congenital human herpesvirus 6 infection. Pediatrics 122, 513–520.

Hubacek, P., Muzikova, K., Hrdlickova, A., Cinek, O., Hyncicova, K., Hrstkova, H., Sedlacek, P., Stary, J., 2009. Prevalence of HHV-6 integrated chromosomally among children treated for acute lymphoblastic or myeloid leukemia in the Czech Republic. J. Med. Virol. 81, 258–263.

Isegawa, Y., Mukai, T., Nakano, K., Kagawa, M., Chen, J., Mori, Y., Sunagawa, T., Kawanishi, K., Sashihara, J., Hata, A., Zou, P., Kosuge, H., Yamanishi, K., 1999. Comparison of the complete DNA sequences of human herpesvirus 6 variants A and B. J. Virol. 73, 8053–8063.

Kondo, K., Kondo, T., Okuno, T., Takahashi, M., Yamanishi, K., 1991. Latent human herpesvirus 6 infection of human monocytes/macrophages. J. Gen. Virol. 72 (Pt 6), 1401–1408.

Leong, H.N., Tuke, P.W., Tedder, R.S., Khanom, A.B., Eglin, R.P., Atkinson, C.E., Ward, K.N., Griffiths, P.D., Clark, D.A., 2007. The prevalence of chromosomally integrated human herpesvirus 6 genomes in the blood of UK blood donors. J. Med. Virol. 79, 45–51.

Linardopoulou, E.V., Williams, E.M., Fan, Y., Friedman, C., Young, J.M., Trask, B.J., 2005. Human subtelomeres are hot spots of interchromosomal recombination and segmental duplication. Nature 437, 94–100.

Morissette, G., Flamand, L., 2010. Herpesviruses and chromosomal integration. J. Virol. 84, 12100–12109.

Nacheva, E.P., Ward, K.N., Brazma, D., Virgili, A., Howard, J., Leong, H.N., Clark, D.A., 2008. Human herpesvirus 6 integrates within telomeric regions as evidenced by five different chromosomal sites. J. Med. Virol. 80, 1952–1958.

Ohye, T., Inagaki, H., Ihira, M., Higashimoto, Y., Kato, K., Oikawa, J., Yagasaki, H., Niizuma, T., Takahashi, Y., Kojima, S., Yoshikawa, T., Kurahashi, H., 2014. Dual roles for the telomeric repeats in chromosomally integrated human herpesvirus-6. Sci. Rep. 4, 4559.

Pellett, P.E., Ablashi, D.V., Ambros, P.F., Agut, H., Caserta, M.T., Descamps, V., Flamand, L., Gautheret-Dejean, A., Hall, C.B., Kamble, R.T., Kuehl, U., Lassner, D., Lautenschlager, I., Loomis, K.S., Luppi, M., Lusso, P., Medveczky, P.G., Montoya, J.G., Mori, Y., Ogata, M., Pritchett, J.C., Rogez, S., Seto, E., Ward, K.N., Yoshikawa, T., Razonable, R.R., 2011. Chromosomally integrated human herpesvirus 6: questions and answers. Rev. Med. Virol. 22, 144–155.

Sedlak, R.H., Cook, L., Huang, M.L., Magaret, A., Zerr, D.M., Boeckh, M., Jerome, K.R., 2014. Identification of chromosomally integrated human herpesvirus 6 by droplet digital PCR. Clin. Chem. 60, 765–772.

Tanaka, N., Kimura, H., Hoshino, Y., Kato, K., Yoshikawa, T., Asano, Y., Horibe, K., Kojima, S., Morishima, T., 2000. Monitoring four herpesviruses in unrelated cord blood transplantation. Bone Marrow Transplant. 26, 1193–1197.

Tanaka-Taya, K., Sashihara, J., Kurahashi, H., Amo, K., Miyagawa, H., Kondo, K., Okada, S., Yamanishi, K., 2004. Human herpesvirus 6 (HHV-6) is transmitted from parent to child in an integrated form and characterization of cases with chromosomally integrated HHV-6 DNA. J. Med. Virol. 73, 465–473.

Thomson, B.J., Dewhurst, S., Gray, D., 1994. Structure and heterogeneity of the a sequences of human herpesvirus 6 strain variants U1102 and Z29 and identification of human telomeric repeat sequences at the genomic termini. J. Virol. 68, 3007–3014.

Ward, K.N., Leong, H.N., Nacheva, E.P., Howard, J., Atkinson, C.E., Davies, N.W., Griffiths, P.D., Clark, D.A., 2006. Human herpesvirus 6 chromosomal integration in immunocompetent patients results in high levels of viral DNA in blood, sera, and hair follicles. J. Clin. Microbiol. 44, 1571–1574.

Yamanishi, K., Okuno, T., Shiraki, K., Takahashi, M., Kondo, T., Asano, Y., Kurata, T., 1988. Identification of human herpesvirus-6 as a causal agent for exanthem subitum. Lancet 1, 1065–1067.

Yoshikawa, T., 2004. Human herpesvirus 6 infection in hematopoietic stem cell transplant patients. Br. J. Haematol. 124, 421–432.

Yoshikawa, T., Suga, S., Asano, Y., Nakashima, T., Yazaki, T., Sobue, R., Hirano, M., Fukuda, M., Kojima, S., Matsuyama, T., 1991. Human herpesvirus-6 infection in bone marrow transplantation. Blood 78, 1381–1384.

Yoshikawa, T., Suga, S., Asano, Y., Yazaki, T., Kodama, H., Ozaki, T., 1989. Distribution of antibodies to a causative agent of exanthem subitum (human herpesvirus-6) in healthy individuals. Pediatrics 84, 675–677.

SCIENTIFIC REPORTS

OPEN

TUBA1A mutation can cause a hydranencephaly-like severe form of cortical dysgenesis

Received: 13 March 2015
Accepted: 16 September 2015
Published: 23 October 2015

Setsuri Yokoi[1,3,*], Naoko Ishihara[2,3,*], Fuyuki Miya[4], Makiko Tsutsumi[1], Itaru Yanagihara[5], Naoko Fujita[1], Hiroyuki Yamamoto[3], Mitsuhiro Kato[6,†], Nobuhiko Okamoto[7], Tatsuhiko Tsunoda[4], Mami Yamasaki[8], Yonehiro Kanemura[9,10], Kenjiro Kosaki[11], Seiji Kojima[3], Shinji Saitoh[12], Hiroki Kurahashi[1] & Jun Natsume[3]

TUBA1A **mutations cause a wide spectrum of lissencephaly and brain malformations. Here, we report two patients with severe cortical dysgeneses, one with an extremely thin cerebral parenchyma apparently looking like hydranencephaly and the other with lissencephaly accompanied by marked hydrocephalus, both harbouring novel *de novo* missense mutations of *TUBA1A*. To elucidate how the various *TUBA1A* mutations affect the severity of the phenotype, we examined the capacity of the mutant protein to incorporate into the endogenous microtubule network in transfected COS7 cells by measuring line density using line extraction in an immunofluorescence study. The mutants responsible for severe phenotypes were found to incorporate extensively into the network. To determine how each mutant alters the microtubule stability, we examined cold-induced microtubule depolymerisation in fibroblasts. The depolymerisation of patients' fibroblasts occurred earlier than that of control fibroblasts, suggesting that microtubules bearing mutated tubulins are unstable. Both mutations are predicted to participate in lateral interactions of microtubules. Our data suggest that the *TUBA1A* mutations disrupting lateral interactions have pronounced dominant-negative effects on microtubule dynamics that are associated with the severe end of the lissencephaly spectrum.**

In the past two decades, it has become evident that the genes encoding cytoskeletal proteins are important in the developing brain[1]. Their importance was initially inferred from the identification of genes encoding microtubule-associated proteins (MAPs), such as *LIS1* (also known as *PAFAH1B1*) and *DCX*, which are mutated in the lissencephaly spectrum[2]. Several years later, new disorders associated with mutations in genes encoding for α- or β-tubulin were described[3–10]. The α- and β-tubulins are the major components of microtubules and are characterised by variable isotypes whose expressions are spatially

[1]Division of Molecular Genetics, Institute for Comprehensive Medical Science, Fujita Health University, Toyoake, Japan. [2]Department of Pediatrics, Fujita Health University School of Medicine, Toyoake, Japan. [3]Department of Pediatrics, Nagoya University Graduate School of Medicine, Nagoya, Japan. [4]Laboratory for Medical Science Mathematics, RIKEN Center for Integrative Medical Sciences, Yokohama, Japan. [5]Department of Developmental Medicine, Research Institute, Osaka Medical Center for Maternal and Child Health, Izumi, Japan. [6]Department of Pediatrics, Yamagata University Faculty of Medicine, Yamagata, Japan. [7]Department of Medical Genetics, Osaka Medical Center and Research Institute for Maternal and Child Health, Osaka, Japan. [8]Department of Neurosurgery, Takatsuki General Hospital, Osaka, Japan. [9]Division of Regenerative Medicine, Institute for Clinical Research, Osaka National Hospital, National Hospital Organization, Osaka, Japan. [10]Department of Neurosurgery, Osaka National Hospital, National Hospital Organization, Osaka, Japan. [11]Center for Medical Genetics, Keio University School of Medicine, Tokyo, Japan. [12]Department of Pediatrics and Neonatology, Nagoya City University Graduate School of Medical Sciences, Nagoya, Japan. *These authors contributed equally to this work. †Present address: Department of Pediatrics, Showa University School of Medicine, Tokyo, Japan. Correspondence and requests for materials should be addressed to H.K. (email: kura@fujita-hu.ac.jp)

and temporally regulated[11,12]. Mutations in a number of neuronally expressed tubulin genes are associated with a spectrum of cortical development malformations commonly referred to as tubulinopathies. These disorders are caused by mutations in *TUBA1A*[3], *TUBB2B*[4], *TUBB3*[5,6], *TUBB*[7], *TUBB4A*[8], *TUBB2A*[9], and *TUBG1*[10] genes. These mutations thought to involve varying degrees of abnormal neuronal proliferation, migration, and postmigrational development that result in a large spectrum of malformations, including lissencephaly, pachygyria, polymicrogyria, and microcephaly[7,11,13].

Microtubules are ubiquitous structural components that contribute to the cytoskeleton, cilia, flagella, axon fibres, and mitotic spindles[14]. Microtubules are dynamic polymers consisting of tandem repeats of α- and β-tubulin heterodimers, which assemble in a head-to-tail fashion at the growing ends of microtubules. Each microtubule is constructed from 13 laterally connected protofilaments of repeating tubulin heterodimers; lateral interactions between each microtubule form the hollow and cylindrical microtubule body[13,15].

TUBA1A gene encoding α1a-tubulin is expressed in almost all post-mitotic neurons throughout neuronal development. *TUBA1A*-related cortical dysgenesis typically shows a posteriorly predominant lissencephaly with cerebellar hypoplasia (LCH), dysmorphic basal ganglia, thin or absent corpus callosum, congenital microcephaly, ventricular dilatation, and abnormalities of the hippocampus and brainstem[16]. However, the clinical phenotypes caused by *TUBA1A* mutations vary considerably. Recently, *TUBA1A* mutations have also been described in perisylvian asymmetrical polymicrogyria[17–19], polymicrogyria-like cortical dysplasia[20], and microlissencephaly in foetal cases[21]. The clinical manifestations of affected patients often include congenital microcephaly, severe intellectual disability, neurodevelopmental delay with diplegia or tetraplegia, and epilepsy[22].

In our study, we performed whole-exome sequencing of two patients with severe cortical dysgeneses. One patient had an extremely thin cerebral parenchyma apparently looking like hydranencephaly, whereas the other had lissencephaly accompanied by marked hydrocephalus. We identified two novel *de novo* heterozygous *TUBA1A* mutations, c.190 C>T (p.R64W) and c.74 G>T (p.C25F). In addition, we performed a functional assay of the mutant proteins to determine why these patients show more severe phenotypes than patients with classical lissencephaly.

Results

Patients' characteristics. Patient 1 (NCU_F41) was a 3-year-old girl. She was born at a gestational age of 37 weeks by caesarean section. Her parents were healthy and unrelated. Her elder sister was also healthy and had normal development. Her mother was referred to our hospital for foetal growth restriction, microcephaly, and marked ventricular dilatation of her foetus on ultrasonography from 28 weeks of gestation. At patient delivery, the amniotic fluid was excessive but the placenta and umbilical cord were normal. Her Apgar scores were 3 and 5 at 1 and 5 min, respectively. She could not breathe spontaneously and needed mechanical ventilation. Her birth weight was 2116 g (−2.0SD), head circumference was 29.6 cm (−2.4SD), and body length was 44 cm (−1.8SD). She had microcephaly, microphthalmos, widely spaced eyes, and micrognathia. Truncal hypotonia with spastic tetraplegia was evident and her digital joints were contractured.

An ophthalmologic examination revealed bilateral optic nerve hypoplasia. Foetal MRI at 28 weeks of gestation and brain MRI at 6 days after birth revealed an extremely thin cerebral parenchyma, hypoplastic brain stem, and agenesis of the cerebellum and corpus callosum (Fig. 1a–d). Test results for toxoplasma, rubella, cytomegalovirus, and herpes simplex (TORCH) infections were negative. Her karyotype was normal 46, XX. After birth, she presented with focal clonic seizures, sometimes with oxygen desaturation. Her electroencephalogram showed extremely poor background activities and focal rhythmic delta waves during the seizures. As the seizures were treated with phenobarbital, they were partially controlled.

At the age of 1 month, a tracheotomy and tracheal separation were performed because of her recurrent aspiration pneumonia. A gastrostomy and fundoplication were also done at the same time. Because of the agenesis of the pituitary, trichlormethiazide for central diabetes insipidus and hydrocortisone and levothyroxine for hypopituitarism were needed. Since her head circumference had been gradually enlarged, a ventriculoperitoneal shunt was placed at the age of 7 months to control the head growth and to assist in nursing care. At 3 years of age, she had spastic tetraplegia and no definite awareness of her environment.

We performed whole-exome sequencing of peripheral blood DNA from the patient and both her parents (Supplementary Fig. S1a). A *de novo* heterozygous c.190 C>T (p.R64W) variant was identified in *TUBA1A*. Subsequent Sanger sequencing confirmed the presence of this variant in the patient 1 and absence in the genomes of both her parents (Supplementary Fig. S2). The c.190 C>T variant was predicted to be damaging by both PolyPhen-2 and SIFT. No potentially pathogenic variants related to malformations of cortical development were identified in any other genes in patient 1 (Supplementary Table S1).

Patient 2 (K3373) was a 2-year-old boy. Ventricular dilatation was identified in the foetal period. His parents were healthy and unrelated. His elder sister was also healthy and had normal development. He was born at a gestational age of 39 weeks by vaginal delivery. His Apgar scores were 8 and 9 at 1 and 5 min, respectively. His birth weight was 2792 g (−0.9SD), head circumference was 33 cm (−0.2SD), and body length was 49.5 cm (+0.3SD). After birth, he was diagnosed with lissencephaly (Fig. 1e–h). He could breathe and swallow by himself. At the age of 8 months, he began suffering from epileptic spasms,

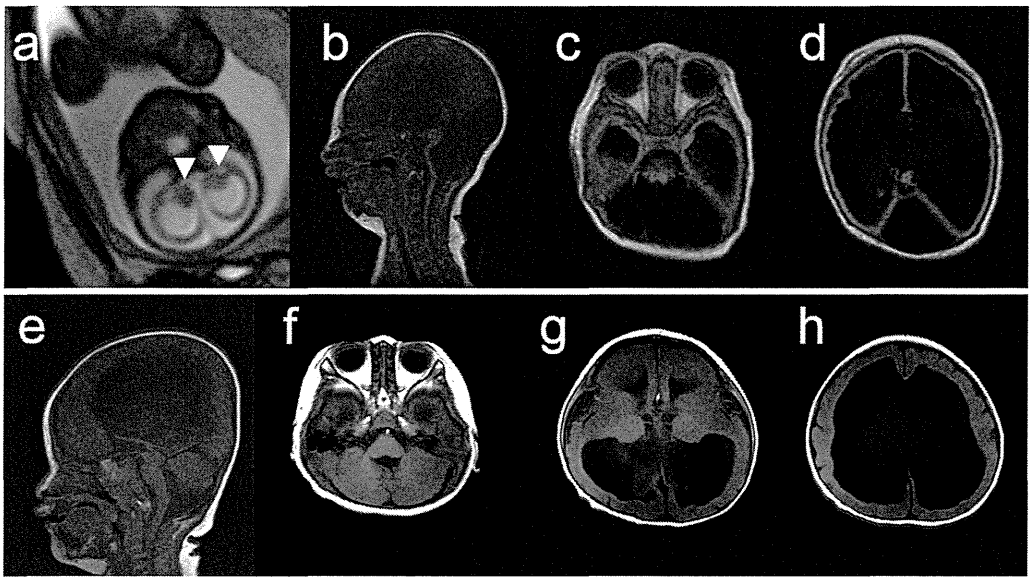

Figure 1. Brain MRI findings of two patients with mutations in *TUBA1A*. (**a**) Foetal MRI at 28 weeks of gestation of patient 1 (T2-weighted image). White arrowheads indicate the basal ganglia. (**b–d**) MRI findings at 6 days after the birth of patient 1 (**b**: T1-weighted image; **c,d**: Fluid Attenuated Inversion recovery [FLAIR]). The patient showed an extremely thin cerebral parenchyma, hypoplastic brain stem, and agenesis of the cerebellum and corpus callosum. Most of the intracranial space was occupied with cerebrospinal fluid. (**e–h**) MRI findings at 1 year of age of patient 2 (T1-weighted images). The patient showed marked ventricular dilatation with a thin cortex, agyria, or limited pachygyria, poorly differentiated dysmorphic basal ganglia, agenesis of the corpus callosum, and slightly hypoplastic cerebellar vermis. The brain stem appeared to be normal.

which could be controlled with sodium valproate and zonisamide. At 2 years of age, he had spastic tetraplegia and was unable to roll over. Although he would not make eye contact and did not speak, he could react to sound and had a smile when his mother called his name.

We performed whole-exome sequencing of peripheral blood DNA from the patient and both his parents (Supplementary Fig. S1b). A *de novo* heterozygous c.74 G>T (p.C25F) variant was identified in *TUBA1A* and confirmed by Sanger methods (Supplementary Fig. S2). This variant was not detected in the genomes of both his parents by Sanger sequencing. The c.74 G>T variant was predicted to be damaging by both PolyPhen-2 and SIFT. There were no potentially pathogenic variants related to malformations of cortical development in any other genes in patient 2 (Supplementary Table S1). Both *TUBA1A* mutations of patients 1 and 2 are located at the amino acids which are conserved across many species (Supplementary Fig. S1c).

Structural modelling of TUBA1A mutations. Both *TUBA1A* mutations reported here are located in the N-terminal domain (Supplementary Fig. S1d) and are predicted to be associated with lateral interactions between microtubules (Fig. 2a–c). According to structural studies conducted using cryoelectron microscopy, protofilaments in microtubules are primarily connected between the M loops and the H1′-S2 and H2-S3 loops[15]. R64 is located on the H1′-S2 loop of α-tubulin (Fig. 2c), which participates in lateral interactions. R64 forms hydrogen bonds with the surrounding residues, E3, F53, and S54 (Fig. 2d). These hydrogen bonds may be involved in the structural stability and/or flexibility of the lateral interactions. Therefore, the R64W mutation is predicted to directly disrupt the lateral interaction. C25 is located on the boundary between helix H1 and the H1-H1′ loop of α-tubulin (Fig. 2c), and this residue faces the luminal side of microtubules (Fig. 2a). The H1-H1′ loop appears to support the H1′-S2 loop and the H2-S3 loop to enhance lateral interactions[15]. Therefore, the C25F mutation may secondarily compromise lateral interactions.

TUBA1A mutants alter the ability of α-tubulin to incorporate into the microtubule network. We examined the ability of the TUBA1A mutants to incorporate into the endogenous microtubule network (Fig. 3). We generated constructs designed to express TUBA1A mutants upon transfection of COS7 cells. The constructs were for wild-type, p.R64W, and p.C25F, as well as p.R402C, which is a recurrent *TUBA1A* mutation that expresses the phenotype of classical lissencephaly, similar to *LIS1* mutations[23]. Transfected cells were examined by immunofluorescence using an anti-FLAG antibody to detect the expression of the transgene and an anti–α-tubulin antibody to detect the overall microtubule network.

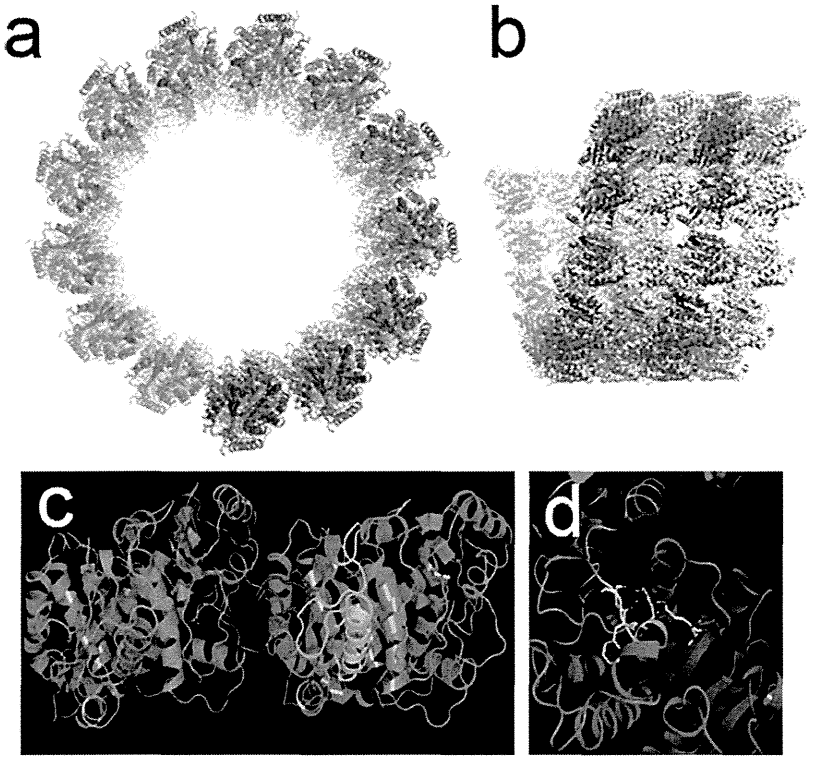

Figure 2. Three-dimensional mapping of *TUBA1A*-mutated residues in a microtubule structure. (**a**) End-on view of a microtubule structural model. A microtubule consists of 13 longitudinal protofilaments that are connected via lateral interactions. α-tubulin molecules are blue, β-tubulin molecules are white, R64 residues are red, and C25 residues are orange. (**b**) Side view of a microtubule. C25 residues are not shown in this view because they are located on the luminal side of a microtubule. (**c**) Higher resolution image of the lateral interaction between the α-tubulin molecules. Both light blue and dark blue are α-tubulin molecules. The M loop is gold, the H1′-S2 loop is red, the H1-H1′ loop is green, and the helix H1 is yellow. The R64 and C25 residues have side chains in this figure. (**d**) The R64 residue forms hydrogen bonds with surrounding residues, E3, F53, and S54.

At 24 h post-transfection, we found that FLAG-tagged wild-type TUBA1A was visualised as lines (Fig. 3a,B) and colocalised with the α-tubulin cytoskeleton (Fig. 3a,C), suggesting that FLAG-tagged wild-type TUBA1A could incorporate into the microtubule network. On the other hand, we found that FLAG-tagged mutant TUBA1A was visible not only as lines, but also as puncta that were diffusely distributed throughout the cytoplasm (Fig. 3a,E,H,K). The linear staining merged with α-tubulin, but the puncta did not colocalise with α-tubulin (Fig. 3a,F,I,L), suggesting that some of the mutant TUBA1A protein could not incorporate into the microtubule network. We observed more incorporated FLAG-tagged TUBA1A protein with R64W and C25F transfection than with R402C. To exclude the influence of the acidic charges of the FLAG tag, we also examined the incorporation of the Myc-tagged TUBA1A protein. Consistent with the data of the FLAG-tagged protein, the incorporation into the microtubule network of Myc-tagged mutant TUBA1A was less than wild-type (Supplementary Fig. S4).

To quantify the incorporation of mutant protein in each transfected cell, we determined the linear staining of FLAG-tagged TUBA1A of each cell by using the ImageJ KBI Line Extract plug-in for line extraction[24] (Supplementary Fig. S3a). These lines indicated the microtubule network of incorporated FLAG-tagged TUBA1A. After line extraction, we measured the total length of the lines and calculated the line density of each cell. The microtubule density of FLAG-tagged TUBA1A for each mutant transfection was analysed.

We found that the microtubule density of FLAG-tagged mutant TUBA1A was significantly lower than that of FLAG-tagged wild-type TUBA1A (Fig. 3b,A). Among TUBA1A mutants, the microtubule density of R64W was the highest, whereas that of R402C was the lowest. We also calculated the microtubule density of α-tubulin in the same manner (Fig. 3b,B). We found that the microtubule density level followed the same order as that of FLAG-tagged TUBA1A. Therefore, the amount of the overall microtubule network tended to depend on the amount of incorporated overexpressed TUBA1A protein. These data indicated that R64W tended to permit higher levels of microtubule incorporation than C25F and R402C. Because there were no significant differences in the mean relative FLAG intensities, the expression levels

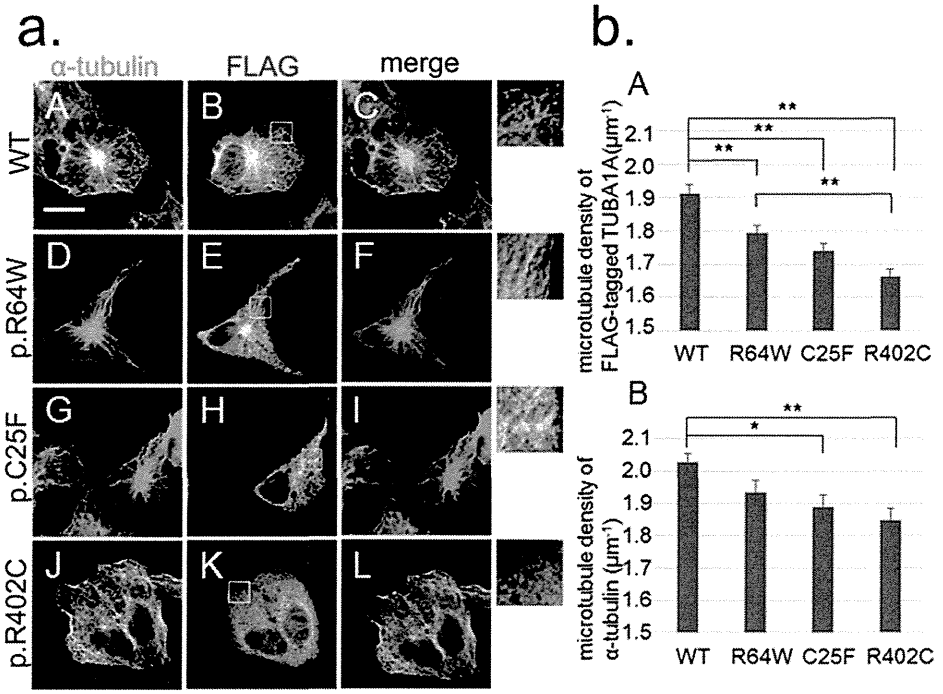

Figure 3. The ability to incorporate into the microtubule network varies among TUBA1A wild-type and mutants. (**a**) Transfected COS7 cells were examined by immunofluorescence using an anti-FLAG antibody (red) and an anti–α-tubulin antibody (green). C-terminal FLAG-tagged wild-type TUBA1A was visualised as lines (B) and colocalised with the cytoskeleton of α-tubulin (C). In the case of FLAG-tagged mutant TUBA1A, there were fewer lines than with the wild-type (E,H,K). Insets are magnified images of the boxes. Scale bar, 20 μm. (**b**) Quantification of microtubule density. We extracted linear staining of FLAG-tagged TUBA1A (A) and the overall cytoskeleton network of α-tubulin (B) of each cell by using the ImageJ KBI Line Extract plug-in and calculated the line density of each cell. Bars represent the means ± SEM (32 cells from wild-type, 28 cells from R64W, 28 cells from C25F, and 31 cells from R402C). Asterisks indicate statistically significant differences (one-way ANOVA and Tukey's post-hoc test; $^{*}p < 0.05$, $^{**}p < 0.01$). (A) The microtubule density of FLAG-tagged mutant TUBA1A was significantly lower than that of FLAG-tagged wild-type TUBA1A. The microtubule density of R64W was the highest among the mutants and that of R402C was the lowest. (B) The microtubule density level of α-tubulin followed the same order as that of FLAG-tagged TUBA1A.

of FLAG-tagged protein in the analysed cells were thought to be similar among wild-type and mutants (Supplementary Fig. S3b).

To assess microtubule dynamics in transfected COS7 cells, we examined repolymerisation after cold induced depolymerisation (Supplementary Fig. S5). There were significantly less cells containing the asters of α-tubulin in the cases of R64W transfection than wild-type (Supplementary Fig. S5c).

TUBA1A mutants alter microtubule stability. We investigated microtubule behaviour in patients' fibroblasts to assess the effects of these mutations on the microtubule stability (Fig. 4). Microtubules of fibroblasts start to depolymerise when they are incubated on ice. We examined the cytoskeleton morphology and the depolymerised tubulin in the fibroblasts by immunofluorescence staining of α-tubulin (Fig. 4a). We first showed by RT-PCR that *TUBA1A* was actually expressed in fibroblasts of the patients and control fibroblasts (control_1) (Supplementary Fig. S6). We defined a cell that contained no linear staining of α-tubulin at 400× magnification to be a completely depolymerised cell. We compared the percentage of completely depolymerised cells between patients' fibroblasts and control ones when they were incubated on ice for 0, 5, 10, 15, and 20 min (Fig. 4b). There were no completely depolymerised control or mutant cells after 0 and 5 min of cold treatment (Fig. 4a,A–F). After 10 min of cold treatment, we found that the percentage of completely depolymerised cells from the R64W and C25F patients was more than four times that of the control (Fig. 4a,G–I,b). The differences for comparison R64W and C25F cells with control cells were statistically significant ($p = 5.6 \times 10^{-24}$ and $p = 5.8 \times 10^{-14}$, respectively, Fig. 4b). This suggested that the depolymerisation of patients' fibroblasts occurred sooner than the control ones. There were almost no differences in the percentage of depolymerised cells after 20 min of cold treatment (Fig. 4a,M–O,b). Repolymerisation of the microtubules could occur in control and mutant

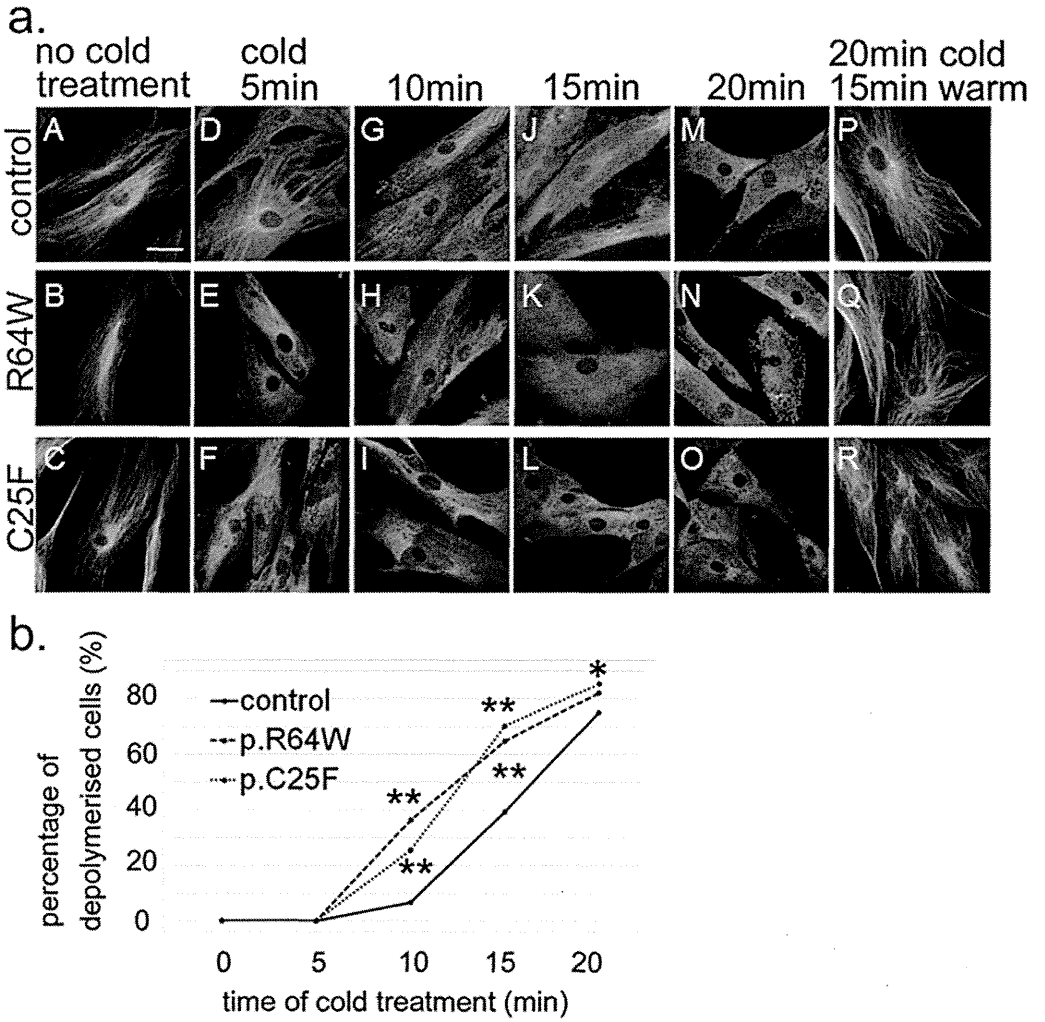

Figure 4. Microtubule behaviour and stability in patients' fibroblasts after various periods of cold treatment. (**a**) Before cold treatment, the cytoskeleton morphologies were similar among control and mutant fibroblasts (A–C). Note that fibroblasts of R64W and C25F were depolymerised after 15 min of cold treatment, whereas polymerised microtubules were still present in control fibroblasts (J–L). Scale bar, 20 μm. (**b**) Percentage of completely depolymerised cells after cold treatment of 0, 5, 10, 15, and 20 min. We counted completely depolymerised cells among 275–400 cells in each condition. After 10 min of cold treatment, the percentage of R64W and C25F fibroblasts showing depolymerisation was more than four times that of control fibroblasts. Asterisks indicate statistically significant differences compared with control (Fisher's exact test and Bonferroni correction using numbers of cells with and without complete depolymerisation, $^{*}p < 0.05$, $^{**}p < 0.0001$).

fibroblasts after treatment on ice for 20 min and subsequently at 37 °C for 15 min (Fig. 4a,P–R) . These data suggested that mutated microtubules are less stable than normal ones.

To assess an underlying mechanism by which *TUBA1A* mutations lead to cortical dysgeneses, we examined the mitosis and the migration of the patients' fibroblasts (Supplementary Fig. S7, S8). There were no significant differences between the patients' and control fibroblasts both in the mitosis and in the migration.

Discussion

In our present study, we identified two novel heterozygous missense *TUBA1A* mutations in patients with severe cortical dysgeneses, one with an extremely thin cerebral parenchyma apparently looking like hydranencephaly and the other with lissencephaly accompanied by marked hydrocephalus. *TUBA1A*-related cortical dysgenesis typically shows a posteriorly predominant lissencephaly with cerebellar hypoplasia (LCH), dysmorphic basal ganglia, thin or absent corpus callosum, congenital microcephaly, ventricular dilatation, and abnormalities of the hippocampus and brainstem[16]. Without these characteristics, it is difficult to determine whether a case with certain brain malformations is a *TUBA1A*-related disorder using

only MRI findings. The brain MRI of our patient harbouring the *TUBA1A* p.R64W mutation manifested an extremely thin cerebral parenchyma with severe hydrocephalus, agenesis of the cerebellum and the corpus callosum, and hypoplastic brain stem, the most severe form of brain malformations. It looked like hydranencephaly but was distinguished from hydranencephaly by the existence of an extremely thin cerebral parenchyma. The cerebral cortex was too thin to assess the layer structure using brain MRI. Thus, our data indicate that the spectrum of *TUBA1A*-related brain malformations is broader than expected.

All previously reported, *TUBA1A* mutations have been heterozygous missense mutations[25,26]. The presence of missense mutations and the absence of nonsense mutations, frameshifts, or whole gene deletions suggest that the mutation results in gain-of-function or has a dominant-negative effect, rather than haploinsufficiency. Among tubulinopathies, it has been proposed that the severity of nervous system impairments may depend on the relative abundance of mutant α- and β-tubulin heterodimers compared with wild-type, combined with their ability to incorporate into the microtubule cytoskeleton, which affect dynamics, motor protein, or MAP interaction in different dominant-negative fashions[13].

In the case of *TUBB3* mutations, R262H substitution permits much more heterodimer formation and microtubule incorporation than R262C, both *in vitro* and in mammalian cells. R262C results in isolated eye movement restrictions, whereas R262H causes not only severe eye movement restrictions, but also other neurological impairments and brain malformations[6]. In the same way, the recurrent R402H mutation in *TUBA1A*, which causes a more severe lissencephaly with complete agyria than R402C, produces a mutant protein that permits higher levels of heterodimer formation and microtubule incorporation than R402C[23,27]. We showed that R64W had the highest amounts of mutant protein incorporation into the network compared with the other mutants and caused the most severe phenotype. In the repolymerisation experiments, the expression of TUBA1A R64W protein impaired the ability of the endogenous α-tubulin to repolymerise. Thus, a greater extent of mutant protein incorporation into the endogenous microtubule network may result in more severe phenotypes in a dominant-negative fashion.

In the current study, the data of the incorporation of FLAG-tagged R402C TUBA1A was different from the previous reports[23,27]. The reason of the difference could be based on the position of the FLAG tag. To exclude the influence of the acidic charges of the FLAG tag, we also examined the incorporation of the Myc-tagged TUBA1A protein. Consistent with the data of the FLAG-tagged protein, limited incorporation of the R402C mutation was observed and the data did not depend on the type of tags. According to the previous report[27], the R402C mutation generated tubulin heterodimers in significantly reduced yield *in vitro* folding reaction. It may be consistent that the R402C mutation disrupts αβ heterodimerisation, leading to little incorporation into the microtubule network.

Tubulin contains three separate structural domains, N-terminal, intermediate, and C-terminal[28] (Supplementary Fig. S1d). These three domains participate in five distinct functions: heterodimer stability, longitudinal and lateral protofilament interactions, nucleotide exchange and hydrolysis, and microtubule–protein interactions[13]. In neurons, lateral interactions are particularly important because microtubules are arranged in dense networks and must be resistant to forces that cause bending or buckling to maintain their structural integrity[13,15,29]. Mutations found at positions essential for lateral interactions are predicted to impede the polymerisation and dynamic properties of microtubules, resulting in microtubules that may be relatively nondynamic or unstable and more likely to depolymerise[13]. In cold-induced depolymerisation of fibroblasts, it is consistent that the two TUBA1A mutants, R64W and C25F, could make microtubules less stable than those of the controls by disrupting lateral interactions.

We investigated the severity of *TUBA1A*-related cortical dysgeneses that are associated with lateral interactions in previous reports as well as in this report. *TUBA1A* mutations that primarily participate in lateral interactions include L286F[30] (M loop), E55K[31], T56M[25], R64W (H1′-S2 loop), and L92V[23] (H2-S3 loop). The patients harbouring L286F, T56M, and L92V were foetuses. Using the classification of Kumar *et al.*[23], four mutations (L286F, T56M, R64W, and L92V) are classified in the severe lissencephaly with cerebellar hypoplasia (LCH severe group 4). On the other hand, E55K belongs to the moderate lissencephaly (LIS moderate group 1) with extreme microcephaly. There are also neighbouring loops that may support lateral interactions. The H1-H1′ loop supports the H1′-S2 loop and the H2-S3 loop, and the end of H6 and the S9-S10 loop appear to stabilise the M loops[15]. *TUBA1A* mutations that secondarily participate in lateral interactions include C25F, E27Q[26] (H1-H1′ loop), Y210C[17], D218Y[23] (the end of H6), G366R[32], A369T[25], and V371E[25] (S9–S10 loop). Five mutations (E27Q, Y210C, D218Y, G366R, and V371E) were classified into the LCH severe group 4 and C25F resembled the LCH severe group 4 phenotype except for milder cerebellar vermis hypoplasia. Only A369T showed central pachygyria. Therefore, many of the reported *TUBA1A* mutations at positions associated with lateral interactions caused severe phenotypes of brain malformations (LCH severe group 4).

In the case of β-tubulin, R62 of TUBB3 is also positioned in the H1′-S2 loop of β-tubulin and is predicted to participate in lateral interactions[6]. However, patients harbouring R62Q have a milder phenotype among TUBB3 mutations. As it was reported that residues involved in lateral interactions cluster in regions of divergence between species and marked difference between α- and β-tubulins[28], there may be different consequences for α- and β-tubulins when lateral interactions are disrupted. We propose that the differences in clinical manifestations among tubulinopathies caused by a mutated tubulin gene should be evaluated.

In conclusion, our data suggest that mutations in *TUBA1A* at positions essential for lateral interactions may lead to severe phenotypes of brain malformations. However, we did not show the consequences

of these mutants for neuronal developmental processes such as proliferation, migration, differentiation, and axonal guidance. In patients' fibroblasts, the mitosis and the migration were not impaired. Further studies of how each mutant affects microtubule function and how it impairs neuronal developmental processes will reveal the precise function of microtubules in normal neuronal development.

Methods

Patients. Genetic testing was approved by the ethical committees of Fujita Health University and collaborated institutes in accordance with the principles of the Declaration of Helsinki, and the Ethical Guidelines for Human Genome/Gene Analysis Research by the Ministry of Education, Culture, Science, and Technology, the Ministry of Health, Labor, and Welfare, and the Ministry of Economy, Trade, and Industry of Japan. Blood samples from affected individuals and their parents, and skin biopsy samples were obtained with informed consent according to local institutional review board guidelines.

Whole-exome sequencing and validation. Genomic DNA was extracted from peripheral blood using the QIAamp DNA Blood Midi Kit according to the manufacturer's instructions (Qiagen, Tokyo, Japan). Three micrograms of DNA were sheared into 150–200-bp fragments using theM220 Focused-ultrasonicator (Covaris, Woburn, MAUSA). To capture the exonic DNA, we used the SureSelect XT Human All Exon V5 capture library (Agilent Technologies, Santa Clara, CAUSA). We then constructed a sequence library using the SureSelect XT Target Enrichment System for the Illumina Paired-End Sequencing Library kit (Agilent Technologies) and performed DNA sequencing of 100-bp paired-end reads using the Illumina HiSeq 2000 sequencer. The sequencing data were mapped to the reference genome (GRCh37/hg19) using BWA (ver.0.6.1). Variant calling was performed using SAMtools (ver.0.1.16) and GATK (ver.1.6) software as previously reported[33]. To identify disease causative mutations, we excluded known variants found in public databases (dbSNP138, 1000 Genomes Project, NHLBI ESP6500, and Exome Aggregation Consortium [ExAC]) and a control in-house database, except for those also identified as pathogenic mutations in the NCBI ClinVar and HGMD databases. We focused on non-synonymous single nucleotide variants (SNVs), insertions and deletions (indels), and splice site variants. Predictions of possible impact of amino acid substitution on the structure and function by variant were performed using PolyPhen-2[34] and SIFT[35] software. The mutations were confirmed by Sanger sequencing.

Structural modelling of TUBA1A mutations. Tubulin dimer structure (PDB ID:1JFF) docked into the density map (MT-13-3, EMDB ID: EMD-5193) using Chimera (https://www.cgl.ucsf.edu/chimera/) after the homology modelling of missing residues 35–60 in α-tubulin was kindly provided by Dr. Haixin Sui, New York State Department of Health[15]. Polymerised microtubule images were then generated with Chimera and MolFeat (FiatLux, Tokyo, Japan).

Transfection experiments. The full-length cDNA encoding the human *TUBA1A* sequence was generated by PCR using a template from placenta cDNA (Forward primer: 5′-TAAGCGGCCGCCATG CGTGAGTGCATCTCCATCCAC-3′, Reverse primer: 5′-TAACTGCAGGTATTCCTCTCCTTCTTCC TCACCCTC-3′). The PCR product was cloned into the *Not* I and *Pst* I sites of the pCMV-4A vector (Agilent Technologies), which is a mammalian expression vector for tagging proteins with a C-terminal FLAG (DYKDDDDK) epitope under the control of the CMV promoter. Three mutations—p.R64W, p.C25F, and p.R402C—were generated by PCR using a template of the wild-type construct. For construction of the Myc tag vectors, the *Xho* I and *Apa* I fragment of these FLAG tag constructs were replaced with a synthesized DNA encoding a Myc tag (The fragment sequence is 5′-TCGAGGAACAAAAACTCATCTCAGAAGAGGATCTGTAGGGCC-3′). All constructs were checked by DNA sequencing.

Constructs were transfected into COS7 cells grown on glass coverslips in Opti-MEM I using Lipofectamine 2000 (Life Technologies). At 24 h after transfection, cells were fixed with ice-cold methanol and stained with a mouse monoclonal anti-α-tubulin antibody (Santa Cruz Biotechnology) and a goat polyclonal anti-DYKDDDDK antibody (Novus Biologicals) at dilutions of 1:250 and 1:5000, respectively. Secondary antibodies were donkey anti-mouse IgG Alexa Fluor 488 and donkey anti-goat IgG Alexa Fluor 594 (Life Technologies) at dilutions of 1:1000. In repolymerisation experiments of COS7 cells[35], cells were incubated on ice for 30 min and then restored to 37 °C for 1.5 min. Cells were immediately fixed with ice-cold methanol and stained as above. For the Myc tag experiment, a rabbit polyclonal anti-Myc antibody (MBL) at dilution of 1:100 and donkey anti-rabbit IgG Alexa Fluor 594 (Life Technologies) at dilutions of 1:1000 were used.

RT-PCR. RT-PCR was done by manufacturer's protocol. NucleoSpin RNA II (MACHEREY-NAGEL) and SuperScript III First-Strand Synthesis System (Life Technologies) were used. The primer sequences of *TUBA1A* and *HPRT* are shown in the Supplementary Figure S6.

Depolymerisation experiments of fibroblasts. Fibroblasts were derived from skin biopsies taken from the patients with p.R64W and p.C25F mutations and control people. The depolymerisation experiments were done as previously described[5]. Briefly, fibroblasts (passage 3) grown on glass coverslips in